Cell tracking -based framework for assessing nowcasting model skill in reproducing growth and decay of convective rainfall

Jenna Ritvanen[1,2], Seppo Pulkkinen[1], Dmitri Moisseev[1,2], and Daniele Nerini[3]

[1]Finnish Meteorological Institute, Helsinki, Finland
[2]Institute for Atmospheric and Earth System Research, Faculty of Science, University of Helsinki, Helsinki, Finland
[3]MeteoSwiss, Locarno-Monti, Switzerland

Correspondence: Jenna Ritvanen (jenna.ritvanen@fmi.fi)

Abstract. The rapid temporal evolution of convective rainfall poses a challenge for quantitative rainfall nowcasting models that forecast rainfall in time scales ranging from 5 minutes to 6 hours. With the growing potential of machine learning models for precipitation nowcasting to produce realistic-looking nowcasts for long lead times, it is important to investigate whether the nowcasts also produce realistic development for convective rainfall. Common verification metrics traditionally used to validate nowcasting models are often dominated by large-scale stratiform rainfall, and averaging the metrics across entire precipitation fields obscures how accurately the models replicate individual convective cells, which makes it difficult to distinguish the model skill for the growth and decay of convective rainfall. In this study, we present a convective cell tracking-based framework to investigate how accurately nowcasting models reproduce the development of convective rainfall. In the framework, a cell identification and tracking algorithm is applied first to the input observation rainfall fields, and then separately to the target observation and nowcast rainfall fields where the tracks identified in the input observations are continued. Features describing the cells and cell tracks, such as the cell volume rain rate and area, are then extracted. In addition to the errors in these feature values, the models' skill in reproducing the existence of convective cells is estimated by calculating several contingency-table metrics, such as the Critical Success Index. The results allow the analysis of how accurately the models reproduce the growth and decay of convective rainfall and quantify the differences between the models, for example, due to differences in how the models smooth the nowcasts, i.e., blurring. The framework also allows differentiation of the results based on the initial conditions of the cell tracks, demonstrated here by separating the tracks into decaying or growing cell tracks based on the cell status when the nowcast is created. We demonstrate the framework with four open-source nowcasting models: the advection nowcast, S-PROG and LINDA models from the pysteps library, and L-CNN model, with data from the Swiss radar network. The results indicate that the L-CNN model reproduced the existence of convective cells best among the models and had smaller errors in the cell volume rain rate than LINDA and S-PROG. LINDA had the smallest underestimation in the cell mean rain rate, whereas S-PROG significantly overestimated the cell volume rain rate and area because of blurring.

1 Introduction

Short-term forecasting from 5 minutes to 6 hours, i.e. nowcasting, of convective rainfall is critical for creating accurate and timely hydrological hazard forecasts and warnings, such as flash flood forecasts (World Meteorological Organization, 2017). Weather radar data are often used to produce rainfall nowcasts for such purposes because of their high temporal and spatial resolution (e.g. 5 min and 1 km; Berne et al., 2004) and their ability to measure surface rainfall better than other remote sensing instruments, e.g., satellite measurements. Accurate quantitative nowcasting of convective rainfall is of special interest, for example, for flash flood modelling, as the highly localised heavy rainfall from convective storms can cause sudden flash floods, especially in urban environments. However, the rapid evolution of convective storms makes nowcasting convective rainfall more difficult than nowcasting low-intensity stratiform rainfall.

Historically, radar-based quantitative rainfall nowcasting has been performed by extrapolating radar echoes (Browning and Collier, 1989). However, because pure extrapolation cannot account for the growth or decay of rainfall, several methods have been developed that, in addition to extrapolation, model the evolution of rainfall, for example, with autoregressive models (Seed, 2003; Bowler et al., 2006; Pulkkinen et al., 2019a, 2020, 2021). In recent years, machine learning (ML) methods have been utilised for radar-based nowcasting. The first ML methods employed recurrent neural networks (RNNs) with convolutional layers or fully convolutional neural networks (e.g., Shi et al., 2015, 2017; Ayzel et al., 2020; Ritvanen et al., 2023). However, with the evolution of the machine learning field, ML nowcasting methods have also evolved, implementing more complicated model architectures, such as attention layers (Trebing et al., 2021), multiple input data sources (Pan et al., 2021; Zhang et al., 2021), and generative models for creating probabilistic forecasts (e.g., Zheng et al., 2022; Ravuri et al., 2021; Leinonen et al., 2023; Zhang et al., 2023).

Convective rainfall poses a challenge for nowcasting methods because of its rapid, non-linear evolution as well as the small spatial scale at which it occurs. In statistical nowcasting methods, such as the S-PROG (Spectral Prognosis; Seed, 2003), small-scale features with poor predictability are usually filtered out to increase the overall forecast performance, which inevitably decreases forecast skill for convective rainfall. Statistical models specially designed for convective rainfall, such as LINDA (Lagrangian Integro-Difference equation model with Autoregression; Pulkkinen et al., 2021), perform better for convective rainfall because of a specifically designed model, but still show blurring in the nowcasts. However, ML methods are expected to predict convective rainfall better because of their ability to implicitly learn non-linear relationships from the large amounts of data used to train the model. While ML models can also suffer from blurring, generative ML models, such as the DGMR (Ravuri et al., 2021), NowcastNet (Zhang et al., 2023), and LDCast (Leinonen et al., 2023) can produce highly realistic-looking nowcasts without blurring also for convective rainfall.

With nowcasting methods producing increasingly realistic nowcasts of rainfall fields for lead times longer than one or two hours, the question remains: how can we verify that the evolution of convective rainfall produced by these methods is also realistic? Thus far, little attention has been paid to this question in nowcasting studies. Often, the forecast skill of nowcasting models and its dependence on rainfall intensity are studied with field-based verification scores calculated either pixel-wise, such as the Critical Success Index (CSI) or Equitable Threat Score (ETS; Schaefer, 1990); or in different-sized neighbourhoods, such

as the Fractions Skill Score (FSS; Roberts and Lean, 2008). These scores are calculated using binary forecasts of exceeding a rain rate intensity threshold. When the threshold value is increased, the number and contiguous areas of pixels that exceed the threshold are reduced. This makes it difficult to discern the source of the error or success in the models. For example, a model

60   that produces otherwise accurate forecasts but with some displacement error would obtain smaller metric values than a model that consistently overestimates the rainfall but is more accurate in location.

    Several previous studies have addressed the issue of decomposing the forecast errors into different components, such as errors in location and intensity, by utilising object-based verification methods. These methods usually apply a contour-based cell identification method with single or multiple thresholds to both the forecast and reference observation fields. Object-based

65   verification methods can be divided into two categories based on whether they 1) compare the fields in which any pixels outside the identified objects are discarded (e.g., Ebert and McBride, 2000; Wernli et al., 2008); or 2) match and compare the individual identified objects between forecasts and observations (e.g., Micheas et al., 2007; Davis et al., 2009; Marzban et al., 2009; Raynaud et al., 2019). While the methods applying the first approach, such as the SAL method (Structure-Amplitude-Location; Wernli et al., 2008), are useful for determining the different sources of forecast error, they are not suitable for

70   investigating how well individual convective cells are forecast, as the error metrics are only calculated on a per-field basis.

    On the other hand, object-based verification methods applying the second approach usually calculate the error metrics separately for each pair of matched objects and can therefore be used to study the forecast error on a per-object basis. The verification results of these methods are usually visualised by either showing the distributions of the error values and/or calculating a single representative value of the errors, such as the mean. These methods have traditionally been applied to numerical

75   weather prediction (NWP) forecasts. For example, the MODE (Method for Object-Based Diagnostic Evolution; Davis et al., 2006a, b) method has been used to study the performance of convection-permitting NWP models (Clark et al., 2014; Mittermaier and Bullock, 2013); ensemble forecasts (Ji et al., 2020); and reanalysis data (Li et al., 2020). Recently, MODE has also been applied to assess nowcasting models (Kong et al., 2023; Ji et al., 2023). The original MODE method identifies the objects of interest only in the spatial domain; however, it has also been extended to the temporal domain in the MODE time-domain

80   (MODE-TD) method. The extension to the time domain has been demonstrated to provide useful information on the evolution of the objects, such as, lifetime, initiation, and dissipation in NWP forecasts (Clark et al., 2014; Li et al., 2020; Mittermaier and Bullock, 2013). Object-based verification has also been applied to verify tropical and extra-tropical cyclone tracks in NWP and data-driven models (Bi et al., 2023; Newman et al., 2023).

    Compared with NWP forecasts and reanalysis data, nowcasts computed by extrapolation of weather radar measurements

85   pose additional challenges and possibilities for object-based verification. First, weather radar data often have higher spatial and temporal resolutions. This allows for the identification and tracking of the objects also in smaller scales, often resulting in a larger number of identified cells. Second, for most weather radar-based nowcasting models, the initial state of the nowcast is the last observation. This allows the comparison of the objects identified in the observations to their counterparts in the nowcasts, and determining also the exact initial state of the objects by tracking them backwards in time. However, in previous

90   nowcasting studies where object-based verification methods have been utilised (e.g., Zahraei et al., 2012; Fox et al., 2016; Li
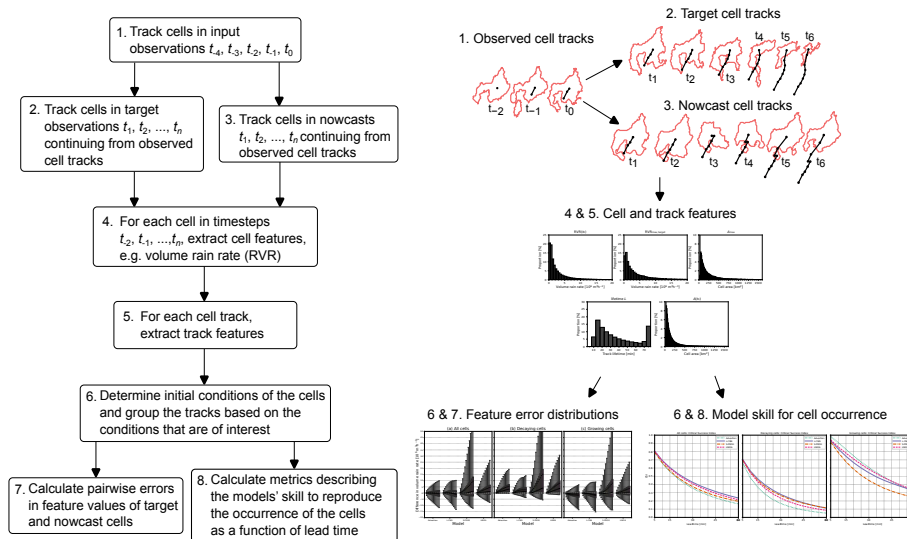
Figure 1. Flowchart of the proposed cell tracking-based framework for studying nowcasting model skill for convective rainfall. The schematic on the left depicts the outputs of the different steps. The cells are (1) tracked first in the input observations, after which the cell tracks are continued in the (2) target observations and (3) in the nowcasts. After that, features describing (4) the cells and (5) the tracks are extracted from the cells. (6) The cell tracks are then differentiated based on initial conditions of interest, and (7) errors for the feature values and (8) metrics describing the cell occurrence are determined.

et al., 2018; Wen et al., 2023; Kong et al., 2023; Ji et al., 2023), the methods have been applied separately to each forecast time step.

In this study, we present a cell tracking-based framework for studying how well the nowcasting models forecast the development of convective cells. An overview of the framework is shown in Figure 1. In the framework, the convective cells that are identified in the input observations are tracked separately in the target observations and the nowcast fields, and the nowcast cells are compared with the observed cells. We demonstrate the framework using four advection-based models: the advection nowcast, S-PROG (Seed, 2003), LINDA (Pulkkinen et al., 2021), and L-CNN (Lagrangian Convolutional Neural Network; Ritvanen et al., 2023). The aim of the framework presented here is to aid model developers in better understanding the models' ability to predict the development of convective rainfall and to verify whether the development is predicted realistically.

The rest of this article is structured as follows. Section 2 describes the data and nowcasting methods that are used in the study. Section 3 presents the framework, and Section 4 describes the results obtained by applying the framework to the data. Finally, Section 5 concludes the study and discusses the implications of the proposed framework.

2 Data and nowcasting models

2.1 Radar data

The rainfall dataset used in this study is the operational radar-only quantitative precipitation estimation (QPE) product from MeteoSwiss for Switzerland (Germann et al., 2006, 2022). The study domain covered by the rainfall product is shown in Figure 2. The rainfall product is produced from radar reflectivity observations using the $Z - R$ relation $Z = 316R^{1.5}$ where the radar reflectivity Z is in linear units of millimetres to the sixth power per cubic meter, and the rainfall rate R is in units of millimetres per hour (Germann et al., 2006; Joss et al., 1998). The data are further processed to remove ground clutter and non-meteorological echoes, correct for visibility and vertical profile of rainfall, and correct for bias compared to rain gauge measurements (Germann et al., 2006), before being stored in an 8-bit format. Furthermore, the data is saturated at approximately $120 \, \mathrm{mm \, h^{-1}}$ (approximately $56 \, \mathrm{dBZ}$).

We used data from May to September from years 2021-2023. From these dates, we applied a selection criterion similar to that in Ritvanen et al. (2023). First, we ranked the dates in descending order according to the number of pixels exceeding $1.0 \, \mathrm{mm \, h^{-1}}$ during the day, and second, we selected the 150 first ranked days as the study material. Furthermore, we split this study dataset into training, validation, and test datasets. The training and validation datasets were used to train the L-CNN model (see Section 2.2.4), and the test dataset was used to perform the analysis. The data was split by first dividing each day into 6 hour blocks. Then, any blocks containing missing data or images with less than 1% pixels larger than $1.0 \, \mathrm{mm \, h^{-1}}$ were removed. The remaining blocks were then randomly divided into training, validation, and test datasets at a ratio of 6:1:5, respectively.

The temporal resolution of the data is 5 minutes, and the spatial resolution is 1 kilometre. The original size of the rainfall fields is 710×640 pixels. However, to obtain an image size that is a multiple of 2^5 in both dimensions, as required by the U-net component of the L-CNN model (Ritvanen et al., 2023; Ayzel et al., 2020), we removed the first six pixels from the left edge, resulting in cropped images of 704×640 pixels. For the analysis presented in this study, we generated nowcasts with each model using the cropped images in the test dataset. The nowcasts were created every 5 minutes for a maximum lead time of 60 minutes with 5-minute time steps.

2.2 Nowcasting models

In this study, four nowcasting models were used: advection nowcast, S-PROG, LINDA, and L-CNN. The models are advection-based, meaning that the motion of rainfall is predicted separately from the temporal evolution of the rainfall. The motion is predicted by extrapolation along a motion field in all four models, but the models differ by how the temporal evolution is predicted in a Lagrangian coordinate system.
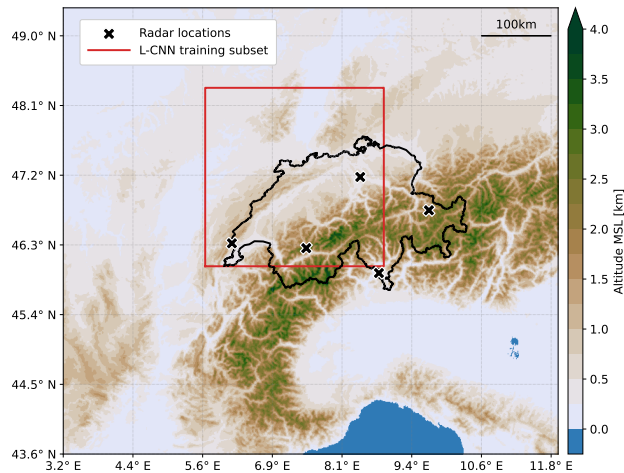
Figure 2. Study domain. The colour indicates the ground altitude in meters above the mean sea level (MSL). The black line shows Switzerland's borders. The bounding box used in training the L-CNN model is shown in red, and the black crosses indicate radar locations.

2.2.1 Advection nowcast

The advection nowcast model, i.e., Lagrangian persistence nowcast, consists of determining the rainfall motion field from previous rainfall fields and then extrapolating the latest observed rainfall field forward in time using the determined motion field. The motion field v is determined using the Lucas-Kanade optical flow (Lucas and Kanade, 1981; Bouguet, 2001) method implemented in the pysteps library (Pulkkinen et al., 2019b; Germann and Zawadzki, 2002). The motion field is determined using 4 previous rainfall fields. We used the default settings for the algorithm (Nerini et al., 2023).

The advection nowcast produces no evolution in the rainfall field. However, there may be small distortions in the fields due to the extrapolation method, and the motion field may contain divergence or convergence that warps the rainfall field. Since the motion fields in this study are calculated from four input fields, the resulting motion field is expected to be smooth in areas with rainfall, while convergence or divergence are more likely at the edges or areas with less rainfall. Therefore, the impact of distortions due to convergence or divergence is likely small at short lead times, when the predicted rainfall is close to its original position, and becomes larger as the lead time increases.

2.2.2 S-PROG

The S-PROG (Spectral Prognosis; Seed, 2003) nowcast model is based on the assumption that the predictability of rainfall depends on the spatial scale of the rainfall. The S-PROG model is calculated by transforming the input rainfall fields to a Lagrangian coordinate system, decomposing the rainfall field into different spatial scales with cascade decomposition, evolving each cascade separately with a lag-2 autoregressive (AR(2)) model, summing the evolved cascade fields and, finally, advecting the summed field to the next time step. In this study, a modified version of S-PROG proposed by Pulkkinen et al. (2019a) is used where AR(2) is applied to the cascade fields in the spectral domain. We used the S-PROG implementation from the

pysteps library (Pulkkinen et al., 2019b; Nerini et al., 2023); for more details on the model refer to Seed (2003), Pulkkinen et al. (2019a) and Pulkkinen et al. (2018).

Owing to the use of AR(2) at multiple spatial scales, the S-PROG model filters out small-scale variations, thereby creating progressively smoother nowcasts. While this improves the skill of the model by filtering out the small scale variability that has poor predictability, it also leads to the blurring of high reflectivity values, that is, convective rainfall.

2.2.3 LINDA

The LINDA (Lagrangian Integro-Difference equation model with Autoregression; Pulkkinen et al., 2021) follows a similar approach to the S-PROG model, but instead of an AR(2) model applied to cascade levels in the spectral domain, the dependence of the predictability of the field on the spatial scale is modelled with a Gaussian convolution-based model and the evolution of the rainfall field through an autoregressive integrated process (ARI(1, 1)). We used the deterministic LINDA model implementation from the pysteps library (Pulkkinen et al., 2019b; Nerini et al., 2023).

The LINDA model implementation allows fitting the parameters of the convolution models and ARI processes separately either to each detected rain cell or to the full rainfall field domain. Although the first approach might perform slightly better for convective rainfall, the difference in performance between the two approaches is not significant (Pulkkinen et al., 2021), and the first approach is much more computationally expensive than the latter. Therefore, in this study we used the latter approach, in which the parameters are optimized for the full domain. Note that the ARI process is still applied separately to each cell.

In previous studies, LINDA has been found to perform better for heavy rainfall than S-PROG (Pulkkinen et al., 2021) or RainNet (Ayzel et al., 2020), a U-net convolutional neural network (CNN) model (Ritvanen et al., 2023). A visual inspection of the nowcasts produced by LINDA (Fig. 3) shows that while LINDA is able to maintain higher rain rates better than S-PROG, it tends to spread the high-intensity areas which leads to blurring in the nowcasts.

2.2.4 L-CNN

The L-CNN (Lagrangian Convolutional Neural Network; Ritvanen et al., 2023) applies a U-net neural network to the temporal difference of rain rate fields. The approach is similar to that of LINDA; however, instead of the ARI and convolution models, the U-net component is used to model the evolution of the temporal difference of rain rate in the Lagrangian coordinates. In a previous study (Ritvanen et al., 2023), this was found to improve, for example, the Equitable Threat Score at short lead times and high rain rate thresholds.

The U-net component of the L-CNN model was trained by using a procedure similar to that in Ritvanen et al. (2023). As described in Section 2.1, the model was trained using the training dataset split, and the convergence of the training was determined using the validation dataset. To speed up the training procedure, we chose a subset of 256×256 pixels from the Swiss rainfall product (see Fig. 2). The L-CNN model was implemented with the PyTorch (Paszke et al., 2019) and PyTorch-Lightning (Falcon and The PyTorch Lightning team, 2019) libraries, and the implementation is available online (Ritvanen, 2024a). Training was performed using a compute node with eight NVIDIA V100 GPUs made available by the Swiss National Supercomputing Centre (CSCS).
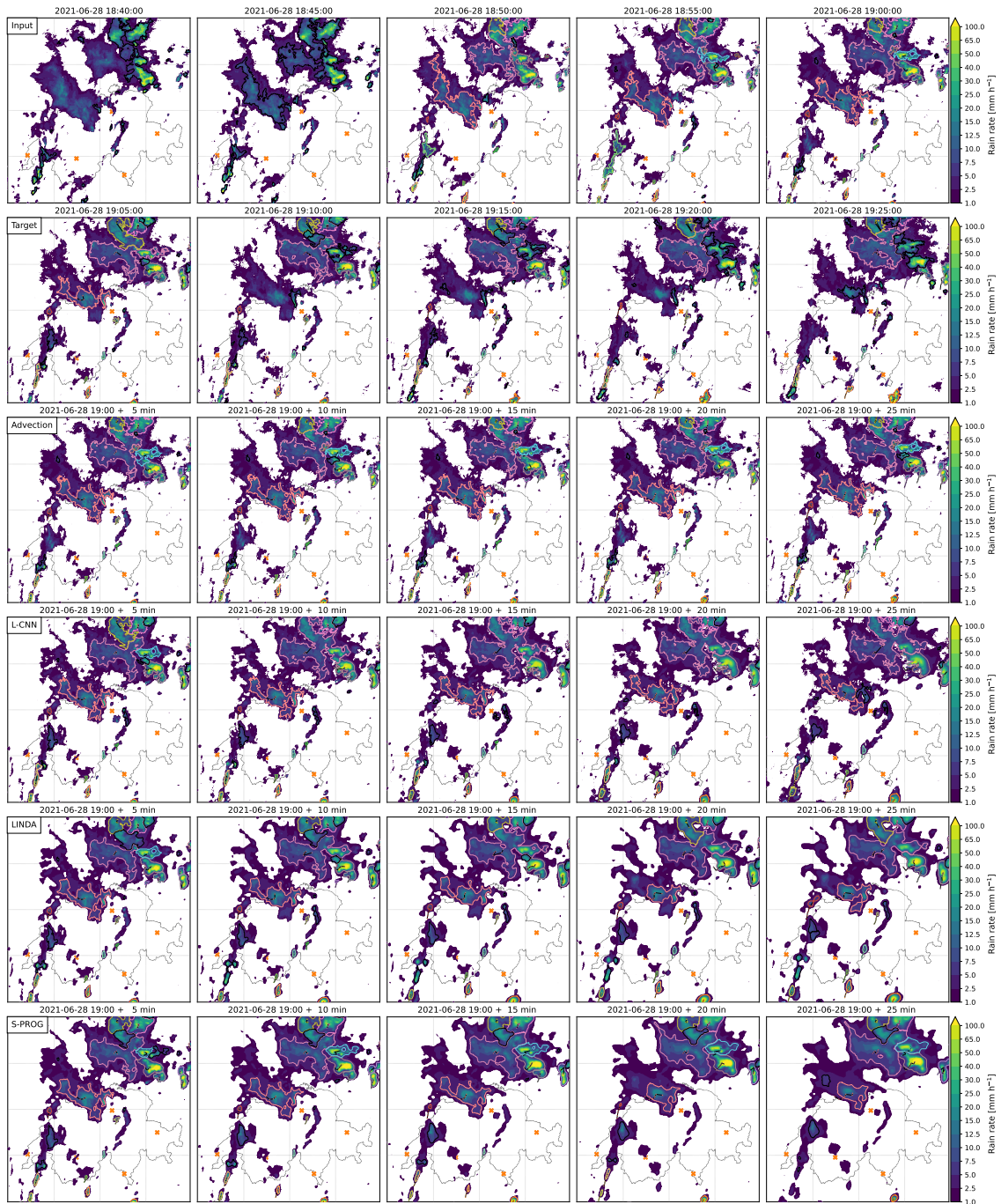
Figure 3. Example of cell tracking results on 28 June 2021 at 19:00 UTC. The panels show the rain rate fields for observations, target observations, and nowcasts. The convective cells identified at that time are plotted in each panel. The cells included in the analysis are shown with coloured contours, with each colour indicating cells belonging to the same track. For each cell track, the cell centroid locations are shown with coloured triangles on top of the black tracks. Cells that were not matched to any track existing at the nowcast creation time step are shown as black contours. The orange crosses indicate the radar locations. Note that panels are zoomed in and do not show the entire domain demonstrated in Figure 2.

3 Cell tracking -based verification framework

In the following sections, we describe the convective cell tracking -based verification framework presented in this study. For the purposes of this study, we define convective cells as all cells that are identified with the contour-based cell identification algorithm where the contours are extracted with a threshold of 35 dBZ, without any further separation based on cell type, and the rainfall inside these cells is considered convective rainfall. The framework (Fig. 1) consists of the following steps:

1. Identify and track the observed cells in the input observations at time steps $t_{-4}, \ldots, t_0$.

2. Continuing from the cell tracks in the input observations, track the observed cells in the target observations at time steps $t_1, \ldots, t_n$.

3. Continuing from the cell tracks in the input observations, track the cells in the nowcast fields at time steps $t_1, \ldots, t_n$.

4. Extract features of all detected cells.

5. Extract track features separately for the cell tracks in target observations and nowcasts.

6. Determine cell track classification into decaying or growing at the nowcast creation time separately for the target and nowcast cell tracks.

7. Calculate error distributions between the feature values in the target and nowcast cells.

8. Calculate metrics describing, for example, the models' ability to reproduce the existence of cells as a function of lead time.

The cell identification and tracking algorithms should be selected to identify and track the cells in a way that is meaningful for the purposes for which the nowcasts are used. Additionally, the algorithms should be able to identify and track the cells in the nowcasts where, depending on the model, the structure of rainfall can vary significantly from the observations. In this study, convective cell identification and tracking were performed using the Thunderstorm Detection and Tracking (T-DaTing) algorithm (Feldmann et al., 2021) implemented in the pysteps library (pySTEPS developers, 2023) and inspired by the thunderstorm radar tracking (TRT) algorithm presented in Hering et al. (2004). The implementation of the cell identification and tracking algorithms is available online at https://doi.org/10.5281/zenodo.11242613 (Nerini et al., 2024).

3.1 Convective cell identification

Convective cells are identified from the rainfall fields in logarithmic radar reflectivity units (dBZ). Because our data are otherwise processed as rain rate in units of millimetres per hour, we first transform the fields into radar reflectivity using the formula $Z = 316R^{1.5}$, where R is the rain rate and Z is the radar reflectivity in linear units of millimetres to the sixth power per cubic meter (Joss et al., 1998; Germann et al., 2006).

After that, we employ the cell identification algorithm (Hering et al., 2004; Feldmann et al., 2021) implemented in the pysteps library (Pulkkinen et al., 2019b). The algorithm begins by discarding all pixels in the rainfall fields below the minimum

reflectivity threshold Z_{min}. From the remaining connected pixel areas, any areas that have peak values less than the peak
reflectivity Z_{p} or smaller than the minimum area threshold A_{min} are discarded. Subsequently, any reflectivity value above the
maximum reflectivity threshold Z_{max} is saturated to that value, and a local maximum detection algorithm (van der Walt et al.,
2014) is used to find the local maxima inside each connected area. The local maxima values are then counted as separate cells
if: i) the path of least change between them decreases by at least ΔZ, and ii) the maxima are located at least d_{min} apart. Cells
within the same connected area are separated using an inverted watershed algorithm (Beucher and Lantuejoul, 1979; van der
Walt et al., 2014).

Since we will compare the features of the identified cells, the selected cell identification method and parameters can poten-
tially impact the results. Table 1 lists the algorithm parameter values used in this study. For the minimum reflectivity Z_{min} and
the maximum reflectivity Z_{max}, the pysteps library default values were used. The peak reflectivity threshold was lowered to
$Z_{\mathrm{p}} = 35$ dBZ, i.e. equal to the cell detection threshold, as we do not want to discard any cells even if the peak reflectivity inside
them would not exceed 35 dBZ. The minimum area threshold was set to $A_{\mathrm{min}} = 25$ km^2 to detect also smaller cells compared
to the work presented by (Feldmann et al., 2021, threshold 50 km^2) as smaller cells are of higher interest to this work (see
Section 4.1). Note that a lower bound for the cell area is required to remove clutter, but the selected value is arbitrary. Finally,
the minimum difference in reflectivity between maxima to be considered separate cells was set to 8 dB and the minimum
distance to 20 km. The selection of these parameters was not as straightforward as their values cannot be directly linked to the
qualities of the identified cells, and because of the algorithm implementation in the pysteps package, the parameter values im-
pact each other and cannot be selected independently. Instead, the values were selected based on an iterative manual process of
comparing the identified cells and cell tracks with different parameter combinations. From the tested parameter combinations,
the selected values produced cell tracks with least "spurious" splits or merges, i.e., situations where large cells with multiple
close-by maxima would be split to multiple cells in a way that is inconsistent between consecutive time steps. Furthermore, a
comparison of the analysis results showed few differences between different parameter combinations.

Table 1. Parameters used for identifying convective cells. The notation follows the algorithm description given in Feldmann et al. (2021).

Variable	Unit	Threshold
Min. reflectivity (Z_{min})	dBZ	35
Max. reflectivity (Z_{max})	dBZ	45
Min. difference in reflectivity (ΔZ)	dB	8
Peak reflectivity (Z_{p})	dBZ	35
Min. area (A_{min})	km^2	25
Min. distance (d_{min})	km	20

3.2 Convective cell tracking

After the convective cells have been identified, cell tracks are established using the tracking algorithm (Hering et al., 2004; Feldmann et al., 2021) by matching them with the cells observed at the next time step. First, the motion of the cells is determined from the current and two previous input rainfall fields using the Lucas-Kanade optical flow algorithm (Lucas and Kanade, 1981; Bouguet, 2001; Pulkkinen et al., 2019b). The cells are then propagated to the next time step along the resulting motion field and compared to the cells observed in the current time step. Any two cells with an overlap greater than 40% are considered the same cell, and are assigned the same identifier. If multiple cells from the previous time step overlap by more than 10% with the same cell, the cell is considered merged; in this case, the identifier of the cell with the largest overlap from the previous timestep is assigned to the new cell and all other cells are considered decayed, if they were not matched with any other cell in the current time step. If one cell overlaps more than 10% with multiple cells at the next time step, the cell track is considered split, in which case the new cell with the largest overlap inherits the identifier of the previous cell, and the cells with smaller overlaps obtain new identifiers.

The result of the tracking algorithm is a list of cell tracks. Because we used two previous rainfall fields to determine the motion of the cells, using input observations from time steps $t_{-4}, \ldots, t_0$ we only obtain cell tracks for time steps $t_{-2}, t_{-1},$ and t_0. For the target observations and nowcasts, we continue the tracking from the cells tracked in the input observations and discard any tracks and cells that are not a continuation of these input observation tracks.

In the analysis presented in Section 4, we use the cell tracks where we consider only the "most representative" cell track, that is, splits and merges in the cell tracks are ignored and the cells with the largest overlap are considered the continuation of the track, as described above. However, because the splits and merges in the cell tracks influence the observed lifecycle of the cells and can therefore potentially impact the analysis, it is important to investigate the extent to which the results are impacted. To this end, we also repeated the analysis using a dataset in which all cell tracks with splits or merges in the input or output observations were removed. In this dataset, all tracks with cells that were the result of a merge of multiple cells, cells that split into multiple cells, or cells that merge with some other cell at the next time step, during either the input or target observations, were excluded. Additionally, all corresponding nowcast cell tracks, that is, nowcast tracks starting from the input cell track of any excluded observed cell track, were also excluded. The relevant results from this dataset are provided in supplementary material, and we discuss the differences in Section 4.5.

While the proposed approach to considering the splits and merges, along with how the "most representative" cell track is defined, is elementary, and other possible approaches and definitions exist, we also note that the nowcasting models used in this study are not expected to reproduce the splits and merges correctly and the blurring occurring in the nowcasts will impact how and at what time step the splits and merges are identified in the nowcasts. Additionally, the number of splits and merges in the dataset is small (see Section 4.5). Therefore, even though this approach might not suffice for statistical analysis of, for example, convective cell lifecycles, for the purposes of this study, i.e., comparative analysis of the selected nowcasting models, the proposed approach is sufficient. A more detailed analysis with more complicated definitions for the "most representative" cell track, for example, by including also the decayed branches of merged cell tracks in the analysis, and analysing how

270 accurately the models reproduce the splits and merges, would be necessary and of interest for models that are expected to reproduce such development in convective cells. Such analysis would most likely also require using cell tracking algorithm with a more advanced processing of splits and merges. For now, we consider a more detailed analysis to be outside the scope of this study.

3.3 Convective cell and track features

275 For each cell in the observations and nowcasts, we determine features to describe the cell:

- Volume rain rate RVR [$m^3\,h^{-1}$]: integrated rain rate over the cell area at a given time step. The definition follows what was used, for example, by Rosenfeld (1987); Hu et al. (2019) and Feng et al. (2018).

- Cell area A [m^2]: area of the cell at a given time step as identified from the rainfall field.

- Mean rain rate R_{avg} [mmh^{-1}]: mean rain rate inside the cell at a given time step.

280 In addition to the features that describe each cell, we determine features describing the cell tracks:

- Lifetime L [min]: observed lifetime of the cell track, that is, the number of time steps the track exists in the input and target observations multiplied by the time step (5 min). Note that because we only obtain cell tracks at three time steps before the nowcast is created and 12 time steps after, the lifetime is saturated to 75 minutes.

- Maximum observed cell area A_{max} [m^2]: maximum observed cell area for a cell track during the time steps where the
285 track exists in the input and target observations.

Only the cell and track features used in the analysis presented in Section 4 are described here. However, depending on the investigated nowcasting models, other features may also be of interest. For example, we do not consider the location of the cells. For advection-based nowcasting models, the error in cell location predicted by the models, defined, for example, through the error in cell centroid location between observed and corresponding nowcast cells, would consist of error in the predicted
290 motion of the cell, i.e., the error in the motion field, and error in the centroid location inside the cell caused by the cell shape. Since the models used in this study use the same motion field and extrapolation method, the first component of the errors would be the same, and therefore any differences between the cell location errors would be small and depend mainly on the cell shape, which would make the location errors difficult to interpret. However, for models in which the cell motion is affected by different factors, the location error can be of interest. Another potentially interesting feature is the maximum rain rate inside
295 a cell; however, for our data, this value is saturated to approx. $120\ \mathrm{mm\,h^{-1}}$ because of the saturation of the original rainfall product, which causes bias in the errors in the maximum rainfall rate.

The aim of the proposed framework is to investigate the ability of the models to predict the development of convective rainfall and the impact of the initial stage of the convective cell. The development of the cell during the nowcast period depends on the stage of the cell when the nowcast is created, that is, whether the cell is growing or decaying. To quantify this, we define
300 for each cell track a status at the nowcast creation time. The status is determined using the derivative of the cell volume rain

rate at nowcast creation time t_0, i.e., $\mathrm{dRVR}_{\mathrm{obs}}(t_0)$. The derivative is estimated using at most the values at $t_{-2}, \ldots, t_2$, of which three values are required to exist for the derivative to be defined. The track status is classified as *growing* if $\mathrm{dRVR}_{\mathrm{obs}}(t_0) > 0$. Conversely, the track status is classified as *decaying* if $\mathrm{dRVR}_{\mathrm{obs}}(t_0) < 0$ or if the track exists at t_0 but not at t_1. In addition to the observations, we determine the status of the cell tracks similarly in the nowcast rainfall fields using $\mathrm{dRVR}_{\mathrm{ncst}}(t_0)$, which is calculated by replacing the RVR values from target observations with the predicted RVR values in the derivative estimation.

3.4 Evaluation of model skill in reproducing convective cell development

The aim of the proposed framework is to study how accurately the nowcasting models reproduce convective cell development. To study this question, we consider the cell tracks (Section 3.2) that exist when the nowcast is created at t_0 and compare the cells in these tracks in the nowcasts to the cells in the corresponding tracks in the target observations. In the results presented later, only the "most representative" cell track was considered, as described in Section 3.2. While this approach discards all cells in tracks newly initiated after t_0 and therefore does not allow the study of new cell formation, it allows us to study the impact of input observations on how well the model reproduces convective cell development. Since a model should be able to predict the evolution of cells that it has seen in the input observations better than that of cells that develop later, the results of this analysis can be considered as the upper limit for model skill in reproducing the development of cells that do not yet exist at the time of nowcast creation.

Table 2. Contingency table for binary forecasts.

	Observed	Not observed	Total
Predicted	Hits (H)	False alarms (F)	$H + F$
Not predicted	Misses (M)	Correct negatives (C)	$M + C$
Total	$H + M$	$F + C$	N

Using this approach, we define the contingency table (Table 2) elements as

- *Hits* (H): cells that exist in both target observations and nowcast

- *Misses* (M): cells that exist in target observations but not in nowcast

- *False alarms* (F): cells that exist in nowcast but not in target observations

- *Correct negatives* (C): cell tracks that existed in the input observations at t_0 and do not exist in target observations or nowcast

Metrics calculated using these definitions for the contingency table elements describe the skill of the model in reproducing the cell occurrence given that the corresponding cell track existed in the input observations. From these values, we calculate as a function of the lead time the metrics Critical Success Index (CSI), Probability of Detection (POD), False Alarm Ratio (FAR),

and Frequency Bias (BIAS), defined as

$$\text{CSI} = \frac{H}{H + M + F} \tag{1}$$

$$\text{POD} = \frac{H}{H + M} \tag{2}$$

$$\text{FAR} = \frac{F}{H + F} \tag{3}$$

$$\text{BIAS} = \frac{H + F}{H + M}. \tag{4}$$

The BIAS values range from zero to infinity, with 1 indicating a perfect score. The other metric values are between 0 and 1; for CSI and POD, the optimal value is 1, and for FAR, the optimal value is 0.

This approach allows us to define the concept of *correct negatives*. However, because the dataset only includes cell tracks that exist at the nowcast creation time, the number of *correct negatives* will be very small compared to the other categories, especially at short lead times. This can lead to unintuitive score values for metrics that utilise *correct negatives*, such as Equitable Threat Score, compared with more balanced datasets. Therefore, we selected to use only metrics that are defined without *correct negatives*.

Another point of interest is how well the models reproduce the cell track classification into a growing or decaying track that describes the initial predicted development of the cell. In the nowcasts, the cell track classification is affected, in addition to the input observations, by the volume rain rate of the nowcast cell in the first two lead time steps, and therefore correct classification would indicate that the model predicts the initial cell development similar to what was observed for that cell.

To study this, we define the cell track classification as a two-category classification problem. For example, in this case a *hit* (H) for the class *decay* (*growth*) would be a cell track whose status is classified as *decaying* (*growing*) in both observations and nowcast. The definitions of *misses* (M), *false alarms* (F), and *correct negatives* (C) follow similarly. Using these, we can estimate the goodness of the classification using different metrics. In addition to the CSI (Eq. 1), POD (Eq. 2), FAR (Eq. 3), and BIAS (Eq. 4), which are calculated separately for both classes, we also use the Equitable Threat Score (ETS; Schaefer, 1990), and the Gerrity score (GS; Gerrity, 1992). The ETS measures the fraction of correctly predicted events accounting for hits due to random chance and is defined as

$$\text{ETS} = \frac{H - H_{\text{r}}}{H + M + F - H_{\text{r}}}, \tag{5}$$

where

$$H_{\text{r}} = \frac{(H + M)(H + F)}{N}, \tag{6}$$

and N is the total number of observation-forecast pairs. ETS obtains values from $-1/3$ to 1, with negative values indicating worse forecast skill than random chance, 0 indicating similar forecast skill as random chance, and 1 indicating a perfect forecast. Note that in this 2-category definition, the ETS value is symmetric between the classes. The Gerrity score is defined as

$$\text{GS} = \frac{1}{N} \sum_{i=1}^{K} \sum_{j=1}^{K} n(F_j, O_i) s_{ij}, \tag{7}$$

where N is the total number of observation-forecast pairs, K is the number of classes (i.e. here $K = 2$), $n(F_j, O_i)$ is the number of forecasts in class j that had observations in class i, and the elements of the scoring matrix s_{ij} are defined as

$$s_{ii} = \frac{1}{K-1}(\sum_{r=1}^{i-1} a_r^{-1} + \sum_{r=1}^{K-1} a_r), \qquad s_{ij} = s_{ji} = \frac{1}{K-1}(\sum_{r=1}^{i-1} a_r^{-1} - (j-i) + \sum_{r=1}^{K-1} a_r), \qquad a_i = (1 - \sum_{r=1}^{i} p_r)/\sum_{r=1}^{i} p_r, \quad (8)$$

where p_i is the observed frequency of class i. The Gerrity score describes the accuracy of the forecast for predicting the correct class considering random chance, and obtains values from $-1 \ldots 1$, with 1 indicating a perfect score.

In addition to the occurrence of convective cells, we are also interested in how accurately different cell and track features are reproduced in the nowcast. To study this, for each pair i of cells in the nowcast and target observations for each lead time t, we calculate the difference of the feature values as

$$\Delta x_i(t) = x_{i,\text{ncst}}(t) - x_{i,\text{target}}(t), \tag{9}$$

where $x_{i,\text{ncst}}(t)$ is the feature value obtained from the cell from the nowcast, and $x_{i,\text{target}}(t)$ is the feature value obtained for the corresponding cell in target observations. If one of the cells does not exist, i.e., the track has died either in the target observations or the nowcast (or both), the cell pair is discarded. From the values $\Delta x_i(t)$, we estimate the mean and median values, i.e. the mean and median errors in feature values, and plot the distributions per lead time and model.

Additionally, we measure the overall predictive capability of the models using the Root Mean Squared Error (RMSE) of the cell volume rain rate, calculated taking into account also the cases where either the target observation cell no longer exists but the nowcast cell exists (*false alarm*), or the target cell exists but the nowcast cell does not (*miss*). In these cases, the volume rain rate of the non-existent cell is taken as zero. Calculated in this way, the error reflects both the model skill in reproducing the cell feature values, as well penalizes the models' inability to reproduce the lifecycle of the cells. The volume rain rate is selected for this error over the other features, as that describes the total rainfall produced by the cell, combining the impact of the cell area and the distribution of rainfall inside the cell. The RMSE is defined as

$$\text{RMSE} = \sqrt{\frac{1}{n} \sum_{i=1}^{n} (\text{RVR}_{i,\text{target}} - \text{RVR}_{i,\text{ncst}})^2} \tag{10}$$

where $\text{RVR}_{i,\text{target}}$ and $\text{RVR}_{i,\text{ncst}}$ are the volume rain rate values of the ith pair of corresponding target and nowcast cells, respectively.

3.5 Evaluation of model skill in reproducing convective cell occurrence

The approach described above does not include information on the formation of new cells or the death of existing cells that are not part of the cell tracks included in the dataset. Rather, this needs to be studied separately. To study the occurrence of the convective cells in the nowcasts, we define it as a binary classification problem: can the convective cell identified in the nowcast be matched to an identified cell in the target observations. A similar approach has been used to verify cell tracking algorithms (e.g., Dixon and Wiener, 1993; Zan et al., 2019; Zhang et al., 2021) and recently for nowcast model evaluation

385 (Wen et al., 2023). Compared to Wen et al. (2023), we evaluate the metrics separately at each lead time, not averaged over all lead times, as it is expected that the model skill for reproducing cell occurrence should decrease as the lead time increases.

To study how well the models reproduce cell occurrence, we consider the cells that have been identified in the target observations and nowcasts, as described in Section 3.1, separately at each lead time step. Note that the cell tracking results are not used here; therefore, all identified cells are considered. Following Wen et al. (2023), the cells in the target observations are

390 matched to the cells in the nowcasts using the Hungarian algorithm (Kuhn, 1955; Crouse, 2016; Virtanen et al., 2020) based on the distance between the cell centroid locations. The result is the combination of matches between the cells that minimises the total sum of the distances between the matched cell centroids. If any match has a distance greater than 20 km, it is considered invalid and the cells unmatched.

The results of this analysis are a set of matched and unmatched cells between the target observations and nowcasts. Next, we

395 define the contingency table elements for this problem. Note that because the problem setting is different from Section 3.4, also the contingency table (Table 2) elements have different definitions; here, for the cell matching without tracking, the elements are defined at each time step after t_0 as

- *Hits* (H): cells that are matched between target observations and nowcast at that time step

- *Misses* (M): cells that exist in target observations at that time step but are not matched to any cell in the nowcast

400  - *False alarms* (F): cells that exist in nowcast at that time step but are not matched to any cell in the target observation

Note that when defining the problem in this way, the category of "correct negatives" has no definition, because we cannot count cells that do not exist in the target observations or the nowcasts.

The metrics calculated from the contingency table elements are defined the same as in Section 3.4 (Eqs. 1-3). However, because the definitions of the contingency table elements differ, the metrics have different interpretations that should not be

405 confused. Here, the metrics describe how well the models reproduce the convective cells that were identified in the observations, without including any information of the cell track history. For a contingency table defined as above, we would expect that a model's increased ability to create new convective rain would result in increased CSI and POD, especially at longer lead times. However, if the model creates too many cells compared to observations, the FAR should increase, indicating a worse skill. Similarly, if the model suppresses cells similar to the observations, the FAR should decrease.

410 ## 4 Results

4.1 Cell track dataset statistics and example case

Figure 4 shows separately for all cell tracks, decaying cell tracks, and growing cell tracks the distributions of cell volume rain rate (Fig. 4a-c) and area (Fig. 4d-f) at the nowcast creation time t_0; the maximum observed cell area (Fig. 4g-i), and the observed track lifetime (Fig. 4j-l). The distributions of the observed cell track lifetime indicate that the division of the cell

415 tracks into decaying or growing tracks is successful: most decaying tracks have an observed lifetime of less than 30 min (note

that the lifetime accounts only for the observed time steps), whereas the lifetime distribution of the growing tracks has fewer values at short lifetimes and a high peak at 75 min, which contains lifetimes of 75 min and longer. The distribution of the $RVR(t_0)$ for the decaying cell tracks (Fig. 4b) shows more cells with small volume rain rates than the growing cell tracks (Fig. 4c). A similar behaviour is observed for cell area $A(t_0)$ (Fig. 4h-i). This is mostly explained by the fact that the decaying

420 category includes cells that exist at t_0 but not at t_1, which also explains the larger number of cells in the decaying category than that in the growing tracks.

Figure 3 shows an example of the nowcasts and convective cell tracking for 28 June 2021 at 19:00 UTC. The panels show the input observations on the first row, the target observations on the second row, and the nowcast rainfall fields on the consecutive rows. Each panel shows the cells identified from the fields, with coloured contours indicating cells that are part of the tracks

425 existing at t_0, and black contours indicating cells that are not part of such tracks.

The nowcasts in Figure 3 demonstrate the features of the different models. For example, the blurring occurring in LINDA and S-PROG as the lead time increases is visible in both the smoothing of the rainfall field and the subsequent smoothing of the cell contours. Additionally, S-PROG shows a clear loss of small cells compared with the other models. While L-CNN does not smooth the nowcast fields as much, it creates much more local decay, which results in uneven cell contour shapes that are

430 visible, for example, in the cells in the bottom-right of the panels.

The case has several small cells that are tracked visually consistently in the input and target observations, for example, in the bottom half of the panels. However, the large cells in the top-right quadrant are split into several cells at certain time steps. Such large cells pose an issue to the identification algorithm because they tend to split "spuriously" into multiple cells if they contain multiple local maxima, as discussed in Section 3.1. The selected cell identification algorithm parameters aim to reduce

435 the number of these "spurious" splits and merges; however, some will still remain in the dataset.

While larger cells are important for nowcasting applications owing to their large hazard potential, in the results presented here, we aim to focus on the smaller cells for several reasons. First, a majority of the cells in the dataset are small; approximately 88% of the cells at the nowcast creation time t_0 have an area smaller than 500 km^2 (Fig. 4d). Second, large convective cells are usually formed of several smaller convective cores, and accurate nowcasting of large cells requires accurate nowcasting

440 of the smaller convective cores. For the models used in this study, the nowcast skill for these convective cores can reasonably be assumed to be similar to that for the individual smaller convective cells. Finally, for large cells, the impact of dislocation error in the pixel-by-pixel verification metrics is smaller than that for small cells; therefore, the large cells would be better represented in these verification metrics. As a result, large cells are a less intriguing research focus for the proposed framework than small cells are.

445 Note that the statistics and results presented here describe convective cells, as they were defined to include radar reflectivities above 35 dBZ, detected from the rainfall product used in the study. Using a different cell identification and tracking methodology or another data product would most likely affect the statistics. Because the data used here are from the Swiss radar network, the climatology of convective rainfall and the convective cells is impacted by orography, for example, the Alps, and as such, the statistics of the convective cells might be different compared to other locations. However, because our aim is
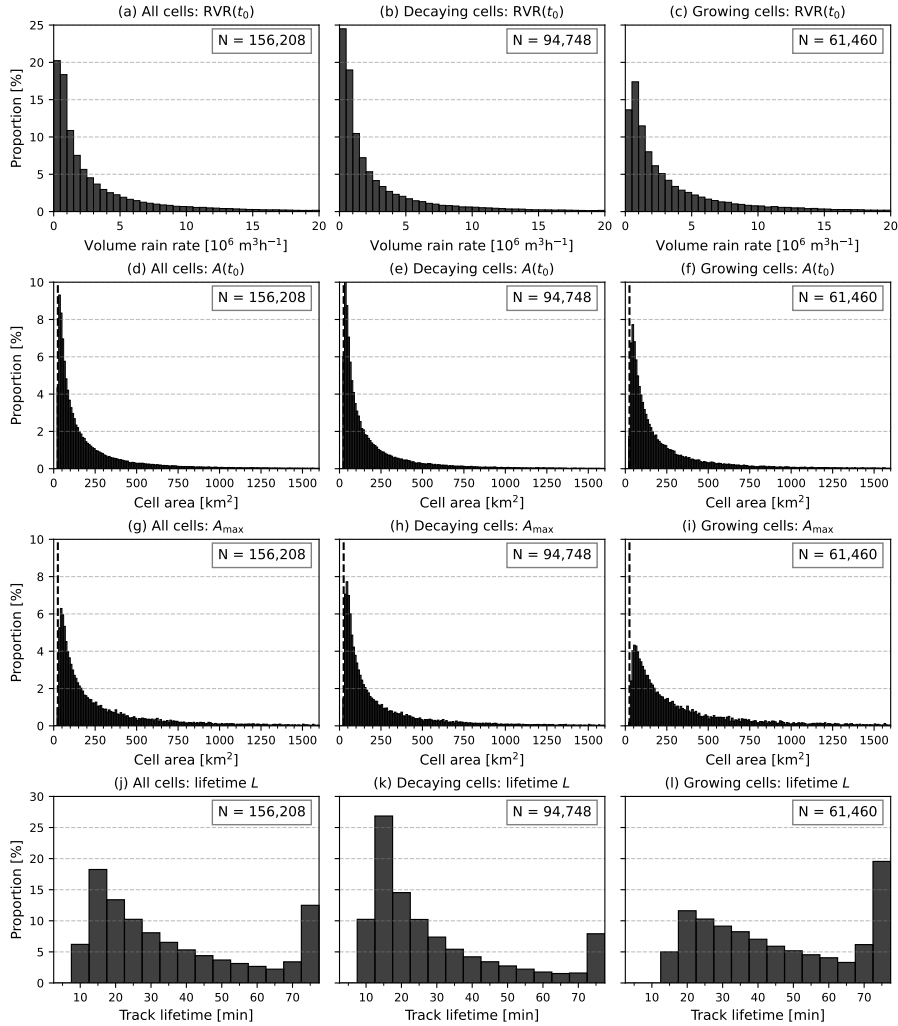
Figure 4. Histograms of cell and track feature values. The panels show (a-c) the volume rain rate at the last observed time step t_0; (d-f) cell area at t_0; (h-i) the maximum observed cell area; and (j-l) the observed cell track lifetime. Histograms are shown for all cells (panels a, d, g), decaying cells (panels b, e, h), and growing cells (panels c, f, i). The value in each panel indicates the number of cells in the histogram. In the cell area histograms (d-i), the vertical dashed line indicates the minimum cell area threshold of 25 km^2.

450   to investigate the performance of the nowcasting models, the statistics of the cell features are mainly used in interpreting the results, and a detailed investigation of the cell statistics themselves is outside the scope of this study.

4.2 Model skill shown by pixel-by-pixel metrics

The common approach to verifying radar-based nowcasting rainfall nowcasting models is using metrics calculated pixel-by-pixel, either contingency-based metrics, such as the Critical Success Index (CSI), or distance-based error metrics, such as the
455   Root Mean Squared Error (RMSE). Figure 5 shows the CSI and RMSE calculated for the models in this study. Both metrics are conditioned on a threshold of $4.6 \mathrm{\ mm\ h^{-1}}$ (corresponding to 35 dBZ, i.e. the cell identification threshold used in the study). For CSI, this means that pixel values below the threshold are considered "no" events, while pixel values at and above the threshold are "yes" events for the contingency table calculation. For the RMSE, the conditioning means that pixels where both the predicted and observed value are below the threshold are excluded from the error calculation.

460   The metrics calculated pixel-by-pixel provide an overview of the model skill. In our data, the L-CNN, LINDA and S-PROG models have almost exactly the same performance in the CSI, while the advection nowcast performs significantly worse. In RMSE, the models have more differences, with L-CNN having the smallest error, and S-PROG and the advection nowcast similar error. Note that LINDA and L-CNN aim to minimise the RMSE between the observations and nowcasts leading to smaller RMSE values than for the advection nowcast and S-PROG. Thus, large part of the RMSE differences can be explained
465   by the varying efficacy of the loss functions in the models, which makes the comparison of RMSE (or any L2-error) unfair. Especially in machine learning models, using a loss function that aims to minimise the prediction error using some other than L2-loss can lead to different trends in L2-errors, while maintaining similar skill in CSI.

Based on these metrics, one might conclude that at the $4.6 \mathrm{\ mm\ h^{-1}}$ (35 dBZ) threshold, the L-CNN model has the best performance and the smallest error in rainfall, with LINDA and S-PROG having similar skill in predicting the exceedance of
470   rainfall at this threshold but with larger errors. Note that any arbitrary threshold gives only a snapshot of the models performance. In this case for CSI, increasing the threshold decreases overall the metric values (see supplementary material Fig. S9); relatively, the performance of S-PROG decreases gradually to a level similar to the advection nowcast, while L-CNN and LINDA perform similarly to each other at every threshold. In RMSE (Fig. S10), increasing the threshold reduces the relative difference between L-CNN and LINDA; the advection nowcast and S-PROG remain similar. However, these metrics, even
475   calculated at multiple thresholds, do not differentiate between various aspects of the models' skill, e.g., whether the models predict the intensity, location, or distribution of heavy rainfall well. Furthermore, the metrics are unable to describe if the model skill depends on the type of rainfall, e.g., if the model is better at predicting decaying than growing rainfall.

4.3 Model skill in reproducing cell development

The main aim of the proposed cell tracking -based framework is to study how accurately the nowcasting models reproduce the
480   development of the identified cells. We measure the comprehensive model skill with the RMSE of the cell volume rain rate, shown in Figure 6. In the RMSE calculation, cells that do not exist in the target observations but exist in the nowcast, or vice versa, are considered zero values. That is, in addition to incorrectly predicted cell volume rain rates, the model is also penalized for cell tracks that decay too fast or slow.
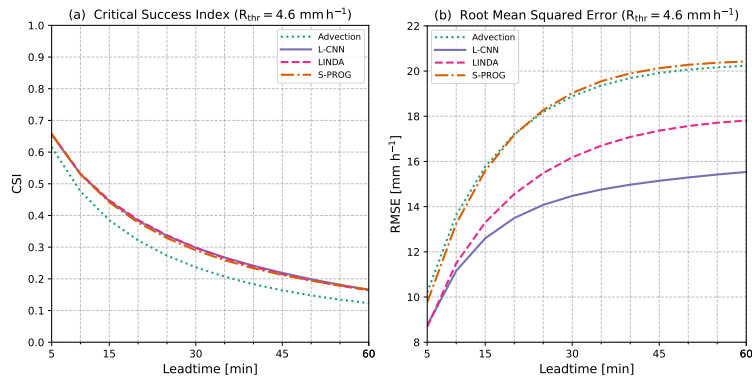
Figure 5. (a) Critical Success Index (CSI) and (b) Root Mean Squared Error (RMSE) calculated from the nowcasts pixel-by-pixel. The metrics are conditioned on a threshold of $4.6\,\mathrm{mm\,h^{-1}}$.

The RMSE is shown separately for all cell tracks, decaying cell tracks and growing cell tracks. Overall, L-CNN and the advection have the smallest errors, while S-PROG has the largest error and LINDA falls between the other models. All models show slightly smaller errors for decaying cell tracks, indicating better predictive skill for decaying cell tracks compared to growing tracks. The difference is the largest for LINDA. The impact of various factors to the model skill is studied further in the following sections by examining separately the model skill for predicting the occurrence of the cells and the feature values of the cells.

Compared to the RMSE calculated pixel-by-pixel (Fig. 5), the major difference in relative errors between the models is the advection nowcast that has significantly smaller error in the cell-based RMSE. Since this error metric does not penalize location errors and the lead times are relatively short, the advection nowcast has small errors, but when the RMSE is calculated pixel-by-pixel and thus location error is penalized, the errors are larger. Another difference between the RMSE values is that in the pixel-by-pixel RMSE (Fig. 5) the error values increase sharply at short lead times and plateau as the lead time increases, while the cell-based RMSE (Fig. 6) increases linearly. In the pixel-by-pixel RMSE, the sharp increase at short lead times is mostly caused by location error. Contrarily, in the cell-based RMSE, the impact of incorrectly predicted cell existence increases as the lead time increases.

4.3.1 Cell existence in tracks

We examine the models' ability to reproduce convective cell development by first focusing on how well the models are able to reproduce the existence of cell tracks. Figure 7 shows the number of cells tracked per lead time and model. The track counts are shown for the entire dataset (Fig. 7a), and divided into decaying (Fig. 7b), and growing tracks (Fig. 7c), as described in Section 3.4. Figure 8 shows the CSI, POD, and FAR metrics calculated from the track counts.

As Figures 7 and 8 only contain cell tracks that existed when the nowcast was created, the advection nowcast shows a very high POD (Fig. 8d-e), as can be expected. Although the advection nowcast obtains a high POD for both decaying and growing
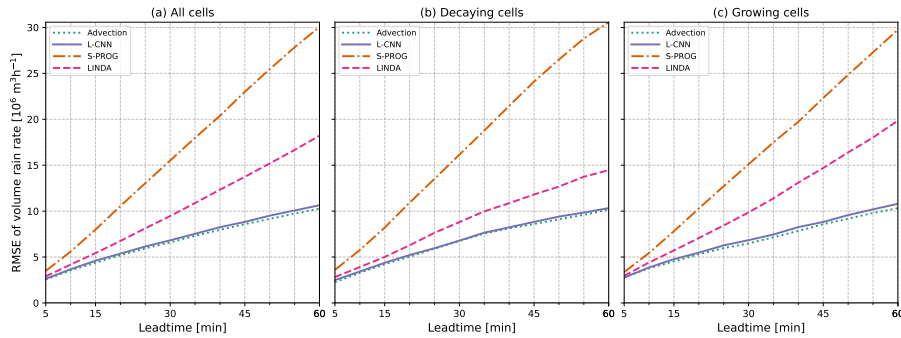
Figure 6. Root Mean Squared Error (RMSE) of cell volume rain rate for (a) all cell tracks, (b) decaying cell tracks, and (c) growing cell tracks. The error has been calculated so that the volume rain rate of non-existing cells in either the target observations or the nowcasts is considered zero. Cell pairs where neither exists were excluded.

505 tracks, the behaviour of CSI values in the two groups is different compared to the other models. For decaying tracks, the advection nowcast obtains the lowest CSI (Fig. 8b) and for the growing tracks, the highest (Fig. 8c). Because the advection nowcast does not produce decay in rainfall, it will overestimate the existence of decaying cell tracks; however, for growing cell tracks, this becomes beneficial. Note also that the advection nowcast obtains the worst FAR in all groups (Fig. 8g-i) but the difference from the other models is larger for decaying cell tracks.

510   S-PROG obtains a lower POD than the other models for these metrics. In CSI, S-PROG performs rather well: similar to LINDA, and only slightly worse than L-CNN for decaying cell tracks. However, S-PROG has significantly worse performance for growing tracks. The high number of misses, low POD, and best FAR, with values similar to those of L-CNN, indicate that S-PROG loses the cells fastest among all the models, most likely due to blurring.

    L-CNN shows the second-largest loss of cells, indicated by the second-worst POD (Fig. 8d-f), FAR similar to S-PROG
515 (Fig. 8g-i), and a high number of misses (Fig. 7). Compared to S-PROG, L-CNN has more false alarms, indicating that the cell tracks do not die as much as in S-PROG, and more hits, leading to higher CSI for both decaying and growing tracks. L-CNN also has the best CSI for all tracks (Fig. 8a), indicating the best overall skill for reproducing the cell track existence, even though the difference from LINDA is small.

    For growing tracks, LINDA has a slightly higher CSI than L-CNN at lead times shorter than 30 min and slightly lower
520 afterwards. LINDA also has the highest POD after advection nowcast for both decaying and growing cell tracks. This indicates that LINDA is the best for reproducing the existence of growing cells and produces less decay than the other models, at the expense of a high number of false alarms and increased FAR (Fig. 8i). For decaying tracks, LINDA has a lower CSI and higher BIAS and FAR than L-CNN, indicating a worse skill in reproducing decay.

    Compared to the CSI calculated pixel-by-pixel (Fig. 5a), the CSI values presented here in Fig. 8a-c show different relative
525 behaviour between the models. The pixel-by-pixel calculated CSI measures the skill in predicting exceedance of rainfall at the 4.6 $\mathrm{mm\,h^{-1}}$ (35 dBZ) threshold and thus penalizes, for example, location error and error in the predicted rainfall values.
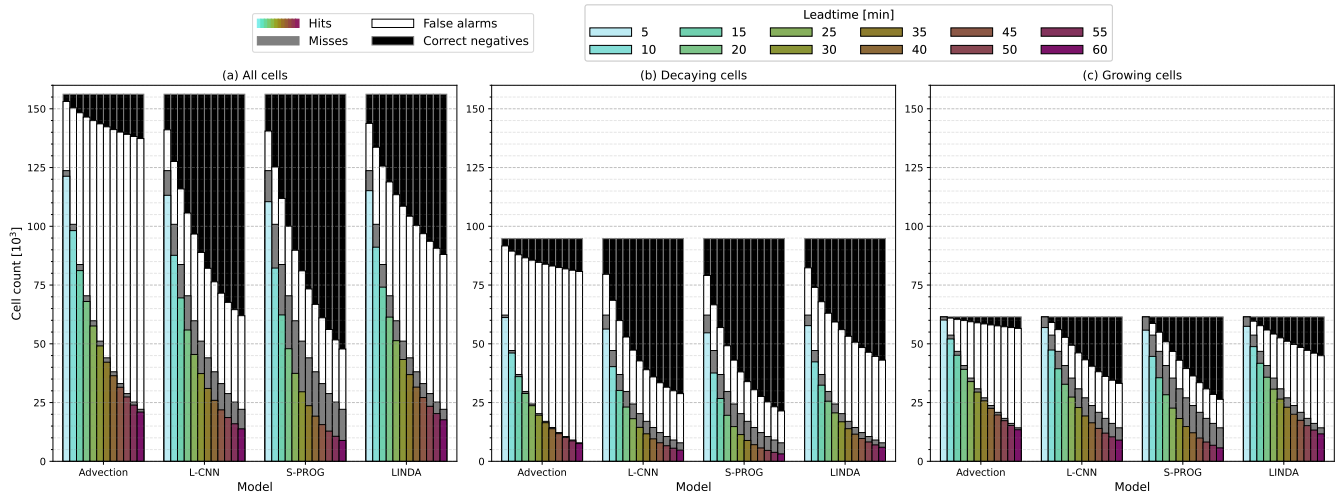
Figure 7. Number of convective cells used in the analysis by nowcast lead time for (a) all cells, (b) decaying cells, and (c) growing cells. Only the cells that are part of the tracks that existed at t_0 are considered. The coloured bars indicate the number of hits, i.e., cells that exist in both target observations and nowcast; the grey bars indicate misses, i.e., cells that exist in target observations but not in nowcast; the white bars indicate false alarms, i.e., cells that exist in nowcast but not in target observations; and the black bars indicate correct negatives, i.e., the number of cell tracks that existed in the input observations at t_0 and do not exist in target observations or nowcast at the given lead time.

However, the CSI of cell track existence measures only how accurately the existence of the cell track is predicted at each lead time, without considering the area or rainfall distribution inside the cells. While in the pixel-by-pixel calculated CSI (Fig. 5a), L-CNN, LINDA, and S-PROG perform similarly, in the cell track CSI we see more differences between the models, as described above, especially when differentiating between decaying and growing cells. As such, the cell track CSI provides more detailed insight into how the models predict convective cells, while the pixel-by-pixel CSI describes overall forecast skill.

4.3.2 Classification to growing and decaying tracks

In addition to the models' ability to reproduce the cell existence, we also study the goodness of the classification to decaying or growing cell tracks in the nowcasts. The classification is affected by the cell volume rain rate at the input time steps and the first two lead time steps, so the goodness of this classification indicates how well the models reproduce the initial cell development.

Figure 9 shows the number of *hits*, *misses*, *false alarms*, and *correct negatives* for the classification (Fig. 9a-b) and classification metric values (Fig. 9c). The ETS and GS metrics indicate the overall goodness of the classification, while the other metrics, calculated separately for growth and decay, show the differences in how well the two stages are predicted at the initial lead time steps. Overall, all models show better values for decay in all separately calculated metrics than for growth. This indicates that all models nowcast the initial decay of convective cells better than initial growth.

Overall, based on the ETS and GS scores, the L-CNN model shows the best skill at reproducing the classification and thus the initial cell development, with LINDA performing only slightly worse. Comparing the metrics calculated separately for
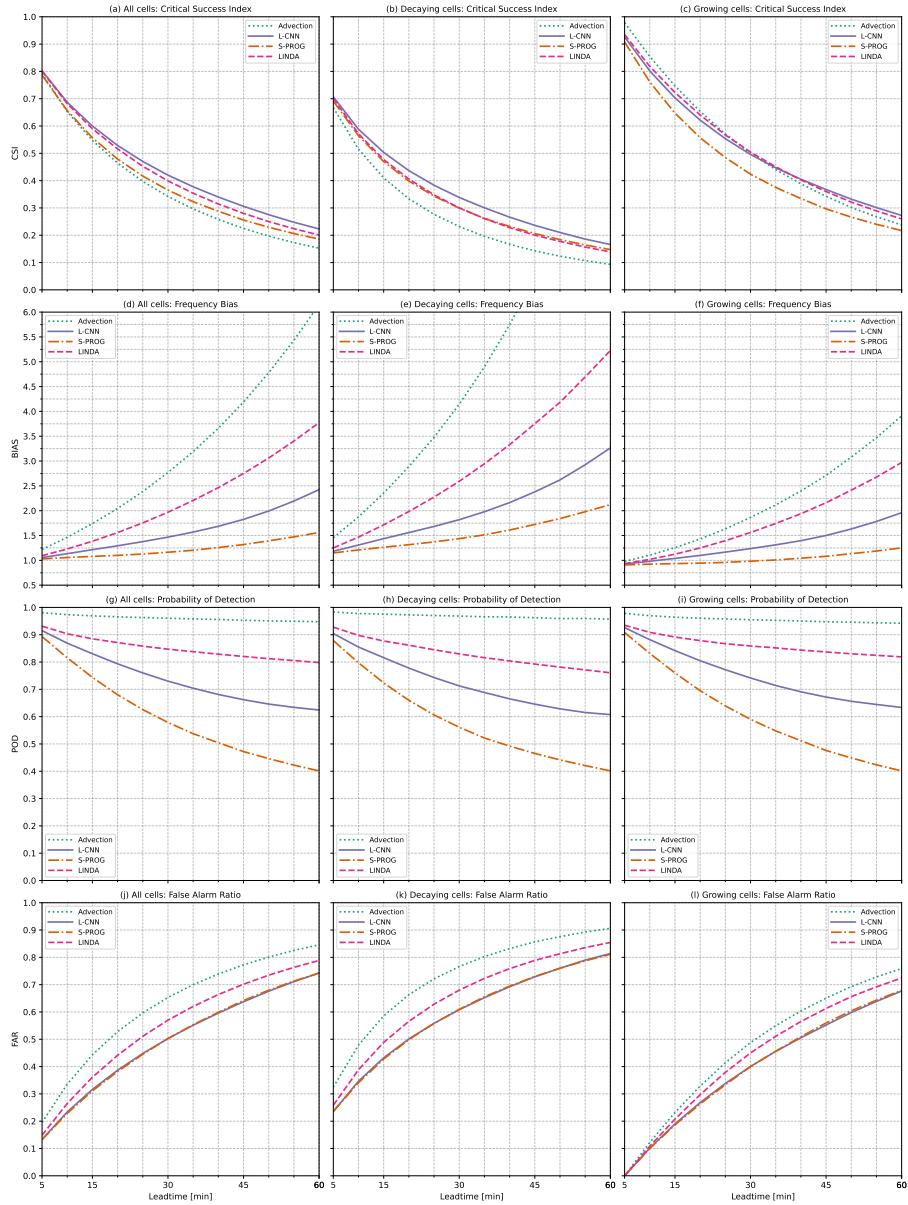
Figure 8. Contingency-based metrics of cell existence as a function of lead time, that is, whether a cell identified in the target observations was also identified in the nowcast. The panels show the Critical Success Index (CSI) for (a) all cell tracks, (b) decaying cell tracks, and (c) growing cell tracks; the Frequency Bias (BIAS) for (d) all cell tracks, (e) decaying cell tracks, and (f) growing cell tracks; the Probability of Detection (POD) for (g) all cell tracks, (h) decaying cell tracks, and (i) growing cell tracks; and the False Alarm Ratio (FAR) for (j) all cell tracks, (k) decaying cell tracks, and (l) growing cell tracks.

growth and decay, the values are similar, with L-CNN obtaining slightly better values than LINDA in all metrics, except CSI for growth and FAR for decay.

545   The advection nowcast obtains the best POD value for the growing tracks. However, because in the advection model the cell RVR values do not change significantly in the nowcast, the RVR derivative, and subsequently the classification, are controlled largely by the observations at and before t_0, and the high POD is most likely explained by this.

S-PROG performs the worst among the models in all metrics except BIAS and POD for the decaying cells. BIAS values close to one indicate a similar number of *misses* and *false alarms*, but, on their own, do not necessarily indicate actual skill.

550   Even though S-PROG has a higher POD for decaying tracks than the advection nowcast, overall S-PROG shows worse skill in reproducing the initial cell development than the advection, that is, persistence, nowcast.
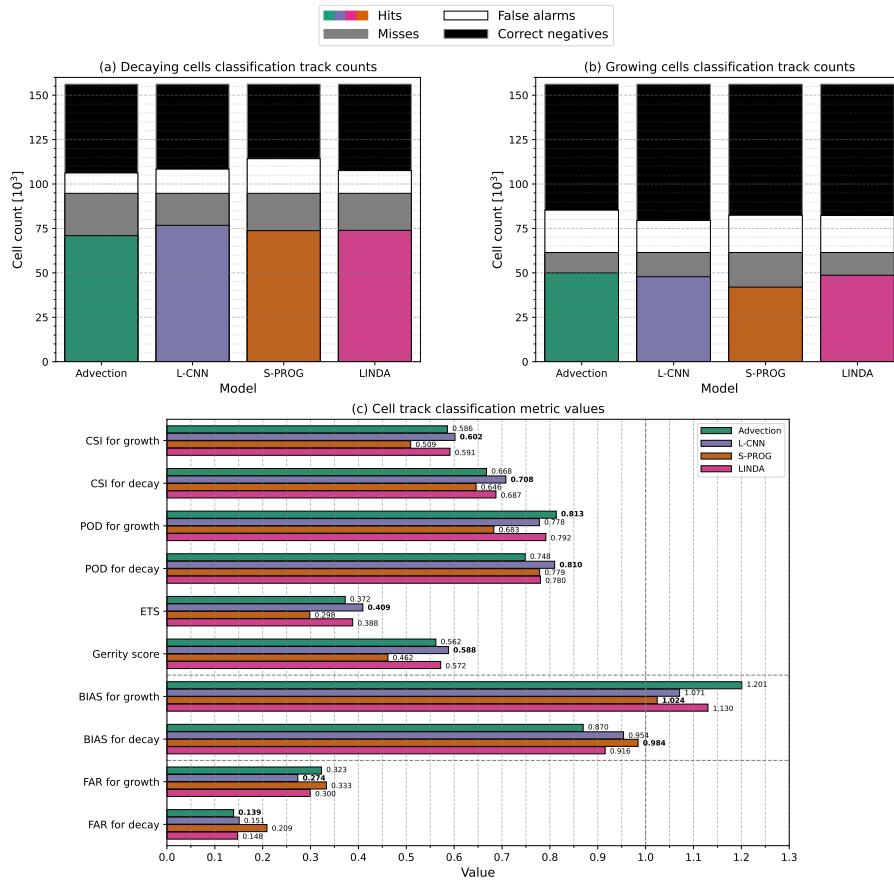
Figure 9. Number of hits (coloured bars), misses (grey bars), false alarms (white bars), and correct negatives (black bars) for the cell track classification into (a) decaying or (b) growing, and (c) contingency table-based metrics of the track classification into decaying or growing for the models. For the Critical Success Index (CSI), Probability of Detection (POD), False Alarm Ratio (FAR), and Frequency Bias (BIAS), the scores are calculated separately for growing and decaying cell tracks by changing the class that is considered the "true" class. For the Equitable Threat Score (ETS) the score is symmetric, and for the Gerrity score (GS), the multicategory version of the score is used; therefore, only one value is provided for both. The best model for each score is marked in the bolded value. For BIAS, the value closest to one, and for FAR, the lowest value are considered best, while for other scores the highest value is the best.

4.3.3 Cell features

Figure 10 shows the error distribution if the cell volume rain rate. The errors in the volume rain rate can be roughly decomposed into the errors in the cell area, shown in Figure 11, and the mean rain rate, shown in Figure 12. The error distributions are shown separately for all cell tracks and for the decaying and growing cell tracks.

For the advection nowcast, the volume rain rate error distributions for all tracks are highly symmetric, and the median and mean errors are close to zero. However, when decomposed into decaying and growing tracks, the fact that the advection nowcast produces no growth or decay results in overestimation in decaying tracks and underestimation in growing. In the cell area error distributions, there is some underestimation of the cell area for all cell tracks as the lead time increases, which largely arises from the growing tracks, as the advection nowcast produces no growth. In the decaying tracks, the advection nowcast has some overestimation of the cell area at short lead times, but the overestimation recedes at lead times longer than 30 min. This could be due to distortions in cell shapes caused by convergence in the motion field. In the mean rain rate, the advection nowcast shows a clear overestimation in both the decaying and growing cell tracks. The tendency for overestimation of the mean rain rate could be caused by large number of small cells in the dataset where the rain rate decreases as the lead time increases, or by irregular rain rate distribution inside cells caused by optical flow interpolation without any smoothing. Nevertheless, the high overestimation of the mean rain rate is compensated by the underestimation of the area, leading to narrower error distribution in the volume rain rate.

The L-CNN model has volume rain rate error distributions that are slightly skewed towards underestimation at longer lead times. This is especially visible in the growing cell tracks. The behaviour of the volume rain rate errors is explained by the opposite behaviours of the cell area and mean rain rate error distributions. The L-CNN produces overestimation in the cell area that increases linearly until 45 min; after which, the overestimation decreases slightly. However, the mean rain rate shows opposite behaviour, with increasing underestimation up to 45 min, after which the mean and median errors plateau. In the mean rain rate, there is little difference between the distributions in the decaying and growing tracks. L-CNN has also smaller median errors in area and volume rain rate than LINDA. This indicates that the localised growth and decay generated by the convolutional neural network in L-CNN can produce more irregular rain rate distributions inside the cells compared to LINDA, that is able to produce only homogeneous development inside the cells due to the Gaussian convolutions in the model. This leads to better estimation of the volume rain rate in L-CNN compared to LINDA.

For S-PROG, the volume rain rate is highly overestimated, mostly because of the large overestimation of the cell areas. This is caused by blurring in the nowcasts, which increases the detected cell size. The wide error distributions are also influenced by the "spurious" splits and merges that occur in large cells (see Section 3.1). In S-PROG, the blurring causes the multiple maxima inside large cells to disappear, leading to more stable cell identification compared with observations that have no blurring, or LINDA and L-CNN, where the blurring is more localised. This leads to an increased number of large errors in the cell area owing to cells that are identified inconsistently in nowcasts and observations. Similar to L-CNN and LINDA, the blurring in S-PROG causes underestimation of the mean rain rate, although the error distributions also have a larger fraction of values with overestimation.
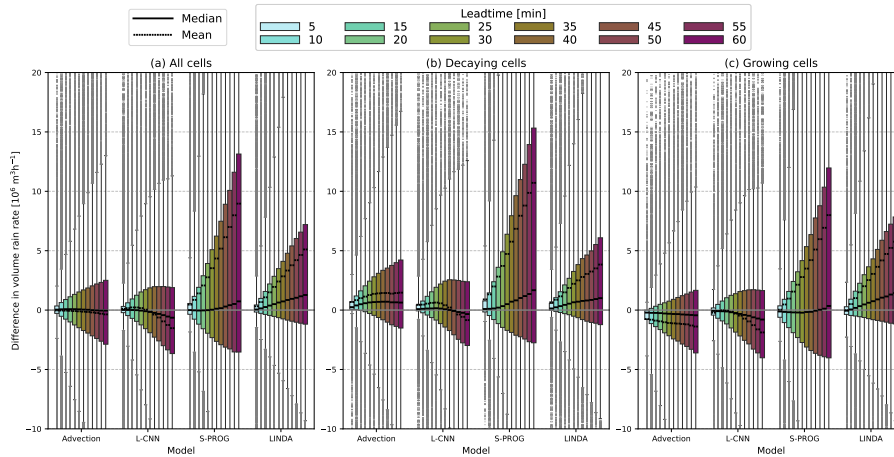
Figure 10. Box plots of differences between predicted and observed cell volume rain rates by nowcast lead time for (a) all cells, (b) decaying cells and (c) growing cells. The boxes show the 25th to 75th percentile range, and the whiskers the 5th to 95th percentile range. The solid line indicates the median and the dotted line the mean, and outliers are indicated by dots. A positive difference indicates overestimation of the volume rain rate by the model, and a negative difference underestimation.

Finally, for LINDA, the volume rain rate is largely overestimated, even though the error distributions are less skewed towards overestimation than for S-PROG. For LINDA, the median error in the volume rain rate is always positive also for growing tracks, indicating that LINDA can produce excessive growth in the cells. In the cell area, LINDA shows overestimation, with very similar distributions for both the decaying and growing tracks. LINDA shows the smallest underestimation of mean 590 rain rate. Most likely, the increased growth in LINDA compensates for the blurring, which leads to slightly a more accurate estimation of the mean rain rate.
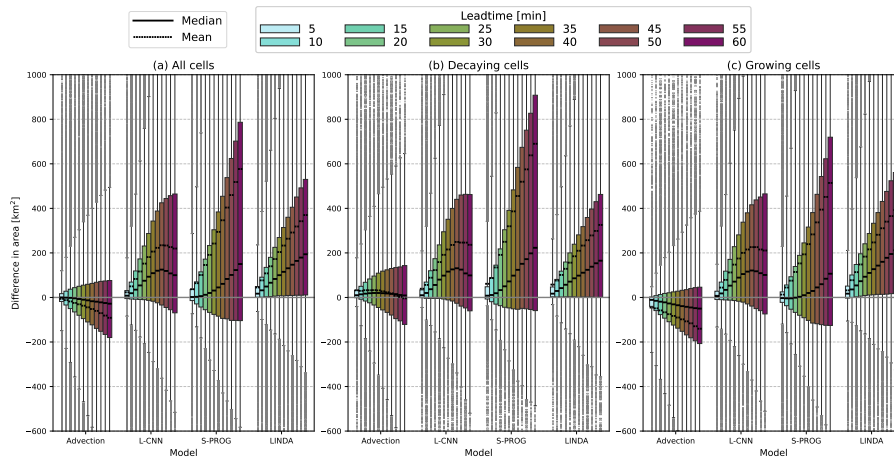
Figure 11. Box plots of differences between predicted and observed cell areas by nowcast lead time for (a) all cells, (b) decaying cells and (c) growing cells. The boxes show the 25th to 75th percentile range, and the whiskers the 5th to 95th percentile range. The solid line indicates the median and the dotted line the mean, and outliers are indicated by dots. A positive difference indicates overestimation of the cell area by the model, and a negative difference underestimation.
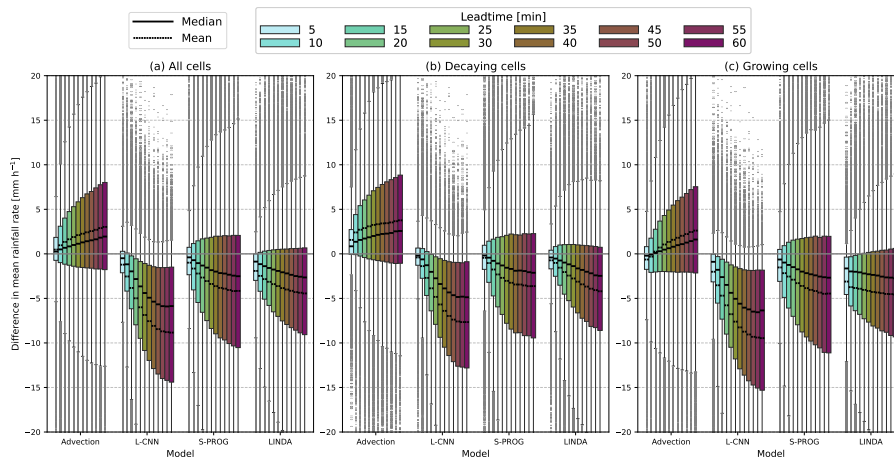
Figure 12. Box plots of differences between predicted and observed mean rain rate inside the cells by nowcast lead time for (a) all cells, (b) decaying cells and (c) growing cells. The boxes show the 25th to 75th percentile range, and the whiskers the 5th to 95th percentile range. The solid line indicates the median and the dotted line the mean, and outliers are indicated by dots. A positive difference indicates overestimation of the mean rain rate by the model, and a negative difference underestimation.

4.4 Model skill in reproducing cell occurrence

As described in Section 3.5, we also study the skill of the models in reproducing convective cell occurrence by identifying the cells at each lead time and matching the cells between target observations and nowcasts. Note that while the metrics presented here are the same as in Section 4.3.1, they have different purposes; here, we are investigating how well the models reproduce the overall cell occurrence, without knowledge of the cell tracks. In this definition, the metrics include also skill for the formation of new cells and the decay of all existing cells.

Figure 13a shows the number of cells identified at each lead time from the nowcasts compared to the target observations, separated to hits, misses, and false alarms, and Figures 13b-e show the metrics calculated from these cell counts. For all models, the number of cells that are matched between the target observations and nowcasts, that is, hits (coloured bars), decreases as the lead time increases. For S-PROG, the decrease as the lead time increases is steeper than for the other models, which indicates that S-PROG is worse at reproducing the cell occurrence than the other models. This is also supported by the clearly lower BIAS values (Fig. 13c), POD (Fig. 13d), and CSI (Fig. 13b) compared to the other models. On the other hand, S-PROG has the smallest number of false alarms, that is, cells that are identified in the nowcast but not matched to any cell in target observations, which is also demonstrated by the low FAR (Fig. 13e).

The other models show a very similar distribution of hits, and therefore, similar CSI. However, the large number of false alarms in the advection nowcast improves POD and worsens FAR. Because the number of identified cells changes very little in the advection nowcast, that is, the number of misses and false alarms are similar, the BIAS for the advection nowcast is close to one at all lead times.

Surprisingly, L-CNN does not show a monotonous trend in the number of false alarms, as is seen for the other models, but instead, the minimum number of false alarms is seen at lead time of 30-35 minutes. This can indicate that the model is generating growth at the later lead times. Compared with LINDA, the decrease in false alarms improves FAR but lowers BIAS and POD, whereas in CSI, the two models perform similarly. Notably, L-CNN and LINDA differ very little in FAR at lead times of 10 min and less. However, for BIAS, L-CNN obtains a value of one at the 5-minute lead time and decreases quickly after that, whereas LINDA has a lower bias value at the 5-minute lead time and a more constant decrease after that. This can indicate that the L-CNN produces little decay at the beginning; however, after the nowcasts begin to decay, it occurs faster than in LINDA, where the decay occurs at a more constant rate.

Comparing the CSI values in Fig. 13b to the CSI values calculated pixel-by-pixel (Fig. 5a) shows some differences. When the CSI is calculated pixel-by-pixel (Fig. 5), the advection nowcast has the worst performance and S-PROG performs similarly to L-CNN and LINDA. However, when calculated using the identified cells, the advection nowcast shows similar performance to L-CNN and LINDA, and S-PROG performs worst. This follows from the different interpretations of the metric. In this cell-based approach, the CSI measures how well the model reproduces the cell existence without considering its exact location (as long as it is close enough to be connected to the cell identified in target observations), shape, or size. From this aspect, the advection nowcast performs well. However, in the pixel-by-pixel framework, CSI describes how well the pixels exceeding

625 the threshold in the nowcast correspond to pixels exceeding the threshold in the observations, and from this aspect, S-PROG performs better due to the blurring increasing the predicted rainfall area.

4.5 Impact of splits and merges in cell tracks

As described previously, the analysis presented in the previous sections used the cell track dataset that included cell tracks with splits and merges. Next, we discuss the impact of splits and merges on the results.

630 Figure 14 shows as a function of lead time the fraction of cells at each lead time that resulted from a cell splitting into multiple cells (split), from multiple cells merging into one (merge), or from both events (see Section 3.2). The fractions are shown separately for the target observations and each nowcasting model. In the target observations, at all lead time steps, there is approximately the same fractions of splits, merges, or both. The fractions increase as lead time increases. This is explained by the increasing fraction of long-living cell tracks in the dataset as the lead time increases, as the dataset includes only tracks

635 that existed at t_0. Long-living cell tracks are more likely to consist of large cells and have splits or merges; as their fraction of the dataset increases, the fraction of splits or merges also increases.

All the nowcasting models clearly reproduce smaller fractions of cells impacted by splits or merges than in the observations, indicating that none of the models could reproduce the splits or merges correctly. The advection nowcast shows approximately constant rates of splits and merges. Because the advection nowcast has no evolution beyond what is caused by convergence or

640 divergence in the motion field, the fraction of splits and merges can be assumed to represent the rate of the "spurious" splits or merges, that is, splits and merges caused by the cell identification algorithm that are inconsistent in time (see Section 3.1). For the other models, the splits and merges are also caused by the evolution of rainfall fields, mainly blurring in the nowcast fields. Because the impact of the blurring on the smoothness of nowcast fields is larger at the beginning, at short lead times, the models produce more splits and merges. The blurring evens the differences between the cells, which results in a larger

645 number of merges than splits. As S-PROG produces most the blurring, it also produces the largest fraction of merges. Notably, compared with S-PROG or LINDA, L-CNN produces approximately the same number of cells impacted by splits, merges, or both, indicating that it reproduces the splits and merges slightly better than the other models.

As described in Section 3.2, we provide as a supplementary material the results repeated for a dataset where the cell tracks containing splits or merges were excluded. Comparing Fig. 4 to Figure S1 shows that approximately 31% (for decaying 25%

650 and for growing 39%) of cell tracks were excluded. The reason for the larger exclusion rate in the growing tracks is that the majority of the excluded cell tracks have a long lifetime and consist of large cells. From the tracks with $RVR(t_0) > 10 \times 10^6$ mm^{3}h^{-1}, 80-90% were excluded, and from tracks with $A(t_0) > 400$ km^2, 60-100% were excluded, while from tracks with a smaller volume rain rate or area at t_0, the percentages of excluded cells were smaller. For the maximum area (Fig. 4g-1), the difference between the datasets is similar to that of $A(t_0)$. In the observed track lifetime, the percentage of

655 excluded cells increases from 13% at 10-minute lifetime to 57 % at 75-minute and longer lead times.

This exclusion of long-living tracks with large cells owing to the splits and merges leads to an overall decrease in the skill for predicting the existence of the cells for all models. Comparing the metrics shown in Fig. 8 to Figure S4, clear decreases in CSI values and increases in BIAS and FAR are visible for all models. For the advection nowcast, L-CNN, and LINDA, the relative
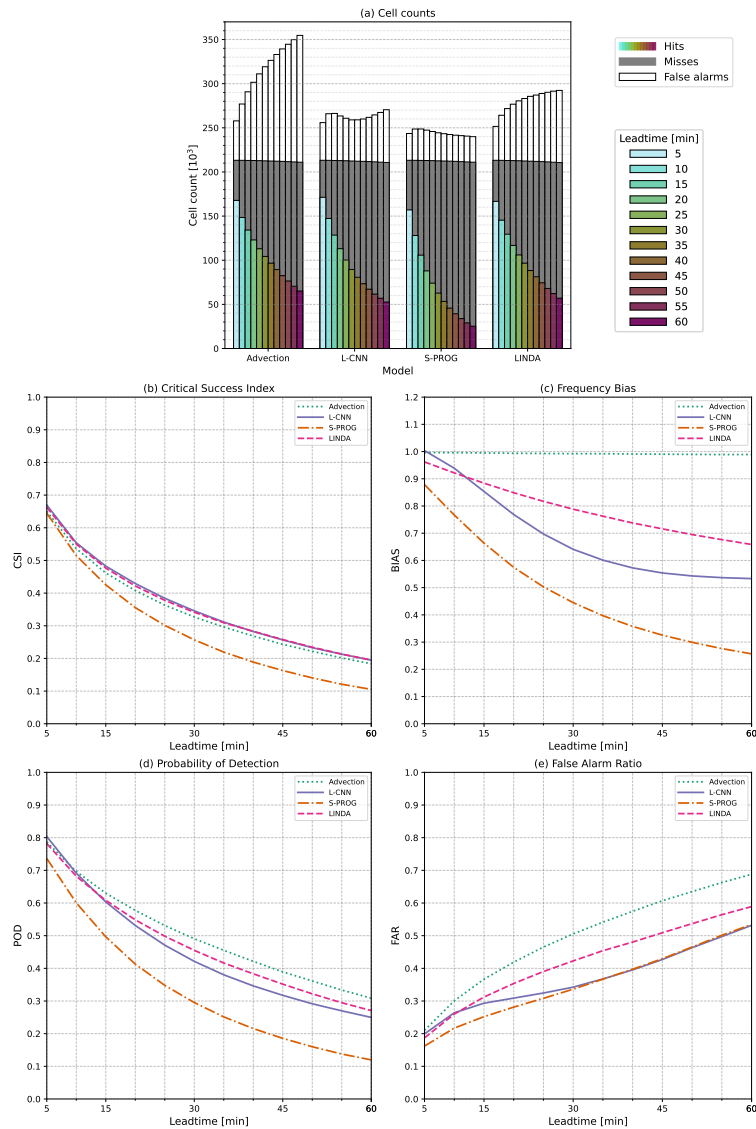
Figure 13. (a) Counts of convective cells by nowcast lead time, and (b) Critical Success Index (CSI), (c) Frequency Bias (BIAS), (d) Probability of Detection (POD), and (e) False Alarm Ratio (FAR) of cell occurrence as a function of lead time, that is, whether a cell that was identified in target observations was matched to a cell identified in the nowcast. Here, cells are detected and matched in the target observations and nowcasts at each lead time separately, i.e., without considering the cell tracks. In panel (a), the coloured bars indicate the number of hits, i.e., cells that exist in both target observations and nowcast; the grey bars indicate misses, i.e., cells that exist in the target observations but are not matched to any existing cell in the nowcast; white bars indicate false alarms, i.e. cells that exist in the nowcast but are not matched to any cell in the target observation. Note that, using this definition, the category of "correct negatives" is not defined. The cells are matched with a Hungarian algorithm based on the distance between cell centroids; any matches that are more than 20 km from each other are discarded.
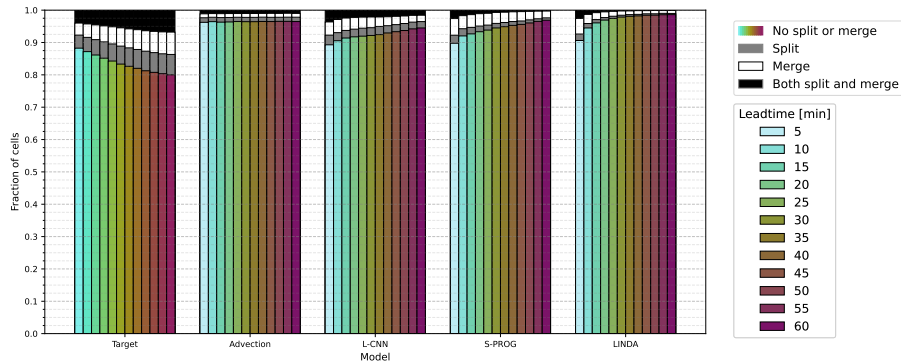
Figure 14. Fractions of splits and merges in the cells as a function of lead time. The coloured bars indicate the fraction of cells that have no splits or merges; gray bars the fraction of cells that are a result of a split; white bars the fraction on cells that have merged from multiple cells; and blacks bars the fraction of cells that result from both a split and a merge. Note that for the target observations and each model, the total number of cells varies.

skill remains similar; however, for S-PROG, an additional decrease in skill is observed compared to the other models. This is
660   particularly visible in the CSI values for all cell tracks and decaying tracks, as well as in the FAR values for all categories. However, for the BIAS values, the other models show higher increases than S-PROG, likely because the large loss of cells due to decay in S-PROG compensates for the increase.

When the cell tracks with splits or merges are excluded, the error distributions of cell feature values (Figures 10-12 and S6-S8) become narrower, and the median and mean errors decrease. This can be attributed to the exclusion of large cells that cause
665   large errors. The narrower distributions are especially visible in the volume rain rate and area; the impact is less visible for the mean rain rate. However, the overall trends in median errors remain similar. Additionally, there are only small differences in the model skill for reproducing the cell track classification at t_0 (Fig. 9 and S5).

Overall, the comparison of the results shows that including tracks with splits and merges improves the model skill in reproducing cell track existence but increases the error in predicted cell features. That is, the models can predict the existence of the
670   "most representative" cell track but not its feature values for cell tracks with splits or merges.

5   Discussion and conclusions

The aim of this study was to develop a framework to investigate how accurately nowcasting models reproduce the development of convective rainfall. The framework consists of identifying and tracking the convective cells in the observations and nowcasts and comparing different cell features between equivalent cell tracks in observations and nowcasts. This approach allows the
675   study of how well the existence of cells is predicted, as well as how accurately the different features of the cells are reproduced by the models. By examining various cell features, such as the cell volume rain rate and area, we can quantify the differences between how the models produce growth and decay in convective rainfall. Furthermore, by tracking cells from the initial obser-

vational inputs used in the models, the framework enables an investigation into how the initial state of convective cells impacts nowcast quality. Compared to standard verification methods, the framework enables separate analysis of various aspects of the nowcasting models' skill for convective rainfall, offering more detailed information to support model development.

The framework was demonstrated using four advection-based, openly available models: advection nowcast, S-PROG, LINDA, and L-CNN. The models were compared using data from the Swiss radar network and a dataset that consisting largely of small convective cells. To investigate the impact of the initial conditions, the cell tracks were classified into tracks that were decaying or growing at the time when the nowcast was created. The results indicate that the advection nowcast can predict the volume rain rate of the cells relatively well, even though it does not create growth or decay in the nowcasts. The L-CNN model was found to best reproduce the existence of convective cells, with a small improvement over LINDA. Even though L-CNN had a slightly smaller error in the cell volume rain rate and area than LINDA owing to the more localised decay predicted by the convolutional neural network in L-CNN, LINDA predicted the cell mean rain rate more accurately. The S-PROG model adequately reproduced the existence of decaying cells, but it also produced the largest overestimations of cell area and volume rain rate.

The proposed framework allowed us to quantify several qualities in the models, such as differences in how L-CNN, LINDA, and S-PROG produce smoothing, which are not easily distinguishable in the pixel-per-pixel verification metrics usually used for nowcasting model validation. Quantifying these aspects of the models aids in model development and in selecting the most suitable nowcasting model for each application. For example, for an application where predicting the volume rain rate correctly is important, such as predicting rainfall accumulation, the L-CNN might be the best among the four models. However, if the correct areal extent of convective rainfall is important, advection nowcast will perform better. Because the models are studied using only the cells identified in the observations and nowcasts, the cell identification and tracking algorithms can be adjusted to describe exactly the convective cells that are significant to the application in question.

However, compared with pixel-by-pixel verification, this framework has certain limitations. Because the dataset is composed of the identified convective cells, the results are sensitive to the selected cell identification and tracking methods, as well as how, for example, splits and merges are processed. Furthermore, the impact of the identification and tracking algorithms can vary between the models, for example if the blurring in the models is different and impacts the cell identification. Additionally, interpreting the results requires expertise in the models studied and knowledge of the underlying dataset, which might make the framework less suitable for use by inexperienced end-users. The complexity of the framework and the sensitivity to selected cell identification and tracking algorithms also make possible comparison between different studies difficult. However, the variety of the results and possibility to adjust the framework provide extensive tools for model developers.

The sensitivity to the selected cell identification and tracking methods and their parameters is also the largest source of uncertainty in the results. Because the methods used here are deterministic, we do not obtain estimates of the uncertainty in identified cells or their tracks. This could be addressed in future research, for example, by estimating the sensitivity of the cells to the identification threshold or other parameters set in the methods. Other sources of uncertainty include the splits and merges occurring in the cell tracks, which can be addressed by estimating the impact of the cell tracks with splits or merges to the results, as was done in this study. Further uncertainty for the framework is caused by uncertainty and errors in the weather radar

observations that can impact the results, for example, through errors in cell identification. This should be addressed foremost through data quality control, as such artefacts in the observations would most likely also reduce the nowcast quality.

715 Because the results are sensitive to the identified cells, adjusting the cell identification and tracking algorithms provides also opportunities for more complex analysis of the models or weather phenomena. These analyses would be especially interesting for models that are able to produce non-smoothed nowcasts, such as generative machine learning models. For example, the models' ability to reproduce the splitting and merging in the cell tracks could be evaluated by applying a cell tracking algorithm that processes the splits and merges in a more sophisticated procedure (e.g., Limpert et al., 2015; Zan et al., 2019). On the other

720 hand, applying a cell detection algorithm capable of identifying cells hierarchically (e.g. Hou and Wang, 2017) would allow evaluating how accurately the models reproduce complex weather phenomena, such as longer-living, multi-cell convective systems.

The presented framework also allows for the study of the impact of the initial conditions of the convective cell on how well its development is predicted. In addition to the initial stage of the cells, which were here divided into decaying and growing

725 stages, another interesting application of the framework would be to study the impact of additional input data sources on the forecast skill. Several studies have shown that additional input data sources, such as numerical weather prediction model data or polarimetric radar measurements, can improve the performance of machine-learning nowcasting models (Sønderby et al., 2020; Pan et al., 2021; Zhu et al., 2022; Lu et al., 2023). The presented framework can be utilised to quantify the impact of data sources on the forecast convective cell development by differentiating the cell tracks based on the data observed in the cells in

730 the input time steps.

The proposed framework is analogous to tropical cyclone tracking used as a verification method, for example, for global ML weather forecasting models (Bi et al., 2023; Newman et al., 2023), applied to high-resolution rainfall forecasts in smaller domains. Although we presented the framework using deterministic models, it can be applied similarly to probabilistic models by applying the cell identification and tracking to each ensemble member separately. In probabilistic models, the ensemble

735 members should be diverse to better capture a wide range of events, and, for example, predicting the correct location of rainfall is not as important as for deterministic forecasts. Because the presented framework considers several aspects of convective cell evolution and is not dependent on the correct location, it can be used to study how well cell evolution is reproduced in ensemble members.

Other possible future developments and applications of the proposed framework would be to extend the cell tracking to cover

740 the entire life cycle of the convective cells, not only the first hour, as was done here. This would be especially interesting when investigating generative machine learning models that can create nowcasts without blurring for long lead times (Ravuri et al., 2021; Zhang et al., 2023). Because the nowcasts do not have blurring and therefore appear realistic to the user, the framework could be used to quantify how realistically the models reproduce convective cell development, and therefore contribute to a greater understanding of the usefulness of such methods when predicting extreme high-intensity rainfall.

Code and data availability. The source code used to produce the pysteps model nowcasts and the analysis in this manuscript is available online at https://doi.org/10.5281/zenodo.14227567 (Ritvanen, 2024b). The source code for training and producing nowcasts with the L-CNN model is available at https://zenodo.org/records/11242483 (Ritvanen, 2024a). The pysteps package version with the updated T-DaTing algorithm, including handling of splits and merges, is available at https://doi.org/10.5281/zenodo.11242613 (Nerini et al., 2024).

The nowcasts and corresponding observations used to run the analysis are available at https://doi.org/10.57707/fmi-b2share.627e6133c2594dc3945d14f6 (Ritvanen et al., 2024a). The analysis results and numerical versions of the result figures are available at https://doi.org/10.57707/fmi-b2share.e1897cfb9a9d4466bb9d7235882bc511 (Ritvanen et al., 2024b). The original MeteoSwiss RZC data used to create the nowcasts and train the L-CNN model are not provided openly because of MeteoSwiss data policy.

Author contributions. All authors contributed in the conceptualization of the study. JR developed the framework, trained the L-CNN model and produced the nowcasts, performed the analysis and wrote the manuscript with input from SP, DM, and DN. SP and DM supervised the project and supported the interpretation of the results. DN provided the Swiss radar data. All authors have accepted the final version of the manuscript.

Competing interests. The authors declare that they have no conflict of interest.

Acknowledgements. JR was funded by a grant from the Vilho, Yrjö and Kalle Väisälä Fund of the Finnish Academy of Science and Letters, and SP was supported by the Academy of Finland project PINCAST (grant no. 341964). The scientific colour maps described in Crameri et al. (2020); Crameri (2023) were used in this study to prevent exclusion of readers with colour vision deficiencies. The colour maps are available at Crameri, F. (2023): Scientific Colour Maps (8.0.1), Zenodo, https://doi.org/10.5281/zenodo.5501399

References

Ayzel, G., Scheffer, T., and Heistermann, M.: RainNet v1.0: A Convolutional Neural Network for Radar-Based Precipitation Nowcasting, Geosci. Model Dev., 13, 2631–2644, https://doi.org/10/gmr9n5, 2020.

765 Berne, A., Delrieu, G., Creutin, J.-D., and Obled, C.: Temporal and Spatial Resolution of Rainfall Measurements Required for Urban Hydrology, Journal of Hydrology, 299, 166–179, https://doi.org/10.1016/j.jhydrol.2004.08.002, 2004.

Beucher, S. and Lantuejoul, C.: Use of Watersheds in Contour Detection, in: International Workshop on Image Processing: Real-time Edge and Motion Detection/Estimation, Rennes, France, 1979.

Bi, K., Xie, L., Zhang, H., Chen, X., Gu, X., and Tian, Q.: Accurate Medium-Range Global Weather Forecasting with 3D Neural Networks, 770 Nature, 619, 533–538, https://doi.org/10.1038/s41586-023-06185-3, 2023.

Bouguet, J.-Y.: Pyramidal Implementation of the Affine Lucas Kanade Feature Tracker Description of the Algorithm, Intel corporation, 5, 4, 2001.

Bowler, N. E., Pierce, C. E., and Seed, A. W.: STEPS: A Probabilistic Precipitation Forecasting Scheme Which Merges an Extrapolation Nowcast with Downscaled NWP, Quarterly Journal of the Royal Meteorological Society, 132, 2127–2155, https://doi.org/10/fc3234, 775 2006.

Browning, K. A. and Collier, C. G.: Nowcasting of Precipitation Systems, Reviews of Geophysics, 27, 345–370, https://doi.org/10.1029/RG027i003p00345, 1989.

Clark, A. J., Bullock, R. G., Jensen, T. L., Xue, M., and Kong, F.: Application of Object-Based Time-Domain Diagnostics for Tracking Precipitation Systems in Convection-Allowing Models, Weather and Forecasting, 29, 517–542, https://doi.org/10.1175/WAF-D-13-00098.1, 780 2014.

Crameri, F.: Scientific Colour Maps (8.0.1), Zenodo, https://doi.org/10.5281/zenodo.5501399, 2023.

Crameri, F., Shephard, G. E., and Heron, P. J.: The Misuse of Colour in Science Communication, Nat Commun, 11, 1–10, https://doi.org/10/ghg5rd, 2020.

Crouse, D. F.: On Implementing 2D Rectangular Assignment Algorithms, IEEE Transactions on Aerospace and Electronic Systems, 52, 785 1679–1696, https://doi.org/10.1109/TAES.2016.140952, 2016.

Davis, C., Brown, B., and Bullock, R.: Object-Based Verification of Precipitation Forecasts. Part I: Methodology and Application to Mesoscale Rain Areas, Monthly Weather Review, 134, 1772–1784, https://doi.org/10.1175/MWR3145.1, 2006a.

Davis, C., Brown, B., and Bullock, R.: Object-Based Verification of Precipitation Forecasts. Part II: Application to Convective Rain Systems, Monthly Weather Review, 134, 1785–1795, https://doi.org/10.1175/MWR3146.1, 2006b.

790 Davis, C. A., Brown, B. G., Bullock, R., and Halley-Gotway, J.: The Method for Object-Based Diagnostic Evaluation (MODE) Applied to Numerical Forecasts from the 2005 NSSL/SPC Spring Program, Weather and Forecasting, 24, 1252–1267, https://doi.org/10.1175/2009WAF2222241.1, 2009.

Dixon, M. and Wiener, G.: TITAN: Thunderstorm Identification, Tracking, Analysis, and Nowcasting—A Radar-based Methodology, J. Atmos. Oceanic Technol., 10, 785–797, https://doi.org/10/dc5g2t, 1993.

795 Ebert, E. E. and McBride, J. L.: Verification of Precipitation in Weather Systems: Determination of Systematic Errors, Journal of Hydrology, 239, 179–202, https://doi.org/10/ch4m9p, 2000.

Falcon, W. and The PyTorch Lightning team: PyTorch Lightning, https://doi.org/10.5281/zenodo.3828935, 2019.

Feldmann, M., Germann, U., Gabella, M., and Berne, A.: A Characterisation of Alpine Mesocyclone Occurrence, Weather Clim. Dynam., 2, 1225–1244, https://doi.org/10.5194/wcd-2-1225-2021, 2021.

800 Feng, Z., Leung, L. R., Houze Jr., R. A., Hagos, S., Hardin, J., Yang, Q., Han, B., and Fan, J.: Structure and Evolution of Mesoscale Convective Systems: Sensitivity to Cloud Microphysics in Convection-Permitting Simulations Over the United States, Journal of Advances in Modeling Earth Systems, 10, 1470–1494, https://doi.org/10.1029/2018MS001305, 2018.

Fox, N. I., Micheas, A. C., and Peng, Y.: Applications of Bayesian Procrustes Shape Analysis to Ensemble Radar Reflectivity Nowcast Verification, Atmospheric Research, 176–177, 75–86, https://doi.org/10.1016/j.atmosres.2016.02.001, 2016.

805 Germann, U. and Zawadzki, I.: Scale-Dependence of the Predictability of Precipitation from Continental Radar Images. Part I: Description of the Methodology, Mon. Wea. Rev., 130, 2859–2873, https://doi.org/10.1175/1520-0493(2002)130<2859:SDOTPO>2.0.CO;2, 2002.

Germann, U., Galli, G., Boscacci, M., and Bolliger, M.: Radar Precipitation Measurement in a Mountainous Region, Quarterly Journal of the Royal Meteorological Society, 132, 1669–1692, https://doi.org/10.1256/qj.05.190, 2006.

Germann, U., Boscacci, M., Clementi, L., Gabella, M., Hering, A., Sartori, M., Sideris, I. V., and Calpini, B.: Weather Radar in Complex
810 Orography, Remote Sensing, 14, 503, https://doi.org/10.3390/rs14030503, 2022.

Gerrity, J. P.: A Note on Gandin and Murphy's Equitable Skill Score, Monthly Weather Review, 120, 2709–2712, https://doi.org/10.1175/1520-0493(1992)120<2709:ANOGAM>2.0.CO;2, 1992.

Hering, A. M., Morel, C., Galli, G., Senesi, S., Ambrosetti, P., and Boscacci, M.: Nowcasting Thunderstorms in the Alpine Region Using a Radar Based Adaptive Thresholding Scheme, in: Proc. Third European Conf. on Radar Meteorology, pp. 206–211, ERAD, Visby, Sweden,
815 2004.

Hou, J. and Wang, P.: Storm Tracking via Tree Structure Representation of Radar Data, J. Atmos. Oceanic Technol., 34, 729–747, https://doi.org/10/f93gwb, 2017.

Hu, J., Rosenfeld, D., Zrnic, D., Williams, E., Zhang, P., Snyder, J. C., Ryzhkov, A., Hashimshoni, E., Zhang, R., and Weitz, R.: Tracking and Characterization of Convective Cells through Their Maturation into Stratiform Storm Elements Using Polarimetric Radar and Lightning
820 Detection, Atmospheric Research, 226, 192–207, https://doi.org/10/ggk6g7, 2019.

Ji, L., Zhi, X., Simmer, C., Zhu, S., and Ji, Y.: Multimodel Ensemble Forecasts of Precipitation Based on an Object-Based Diagnostic Evaluation, Monthly Weather Review, 148, 2591–2606, https://doi.org/10.1175/MWR-D-19-0266.1, 2020.

Ji, Y., Gong, B., Langguth, M., Mozaffari, A., and Zhi, X.: CLGAN: A Generative Adversarial Network (GAN)-Based Video Prediction Model for Precipitation Nowcasting, Geoscientific Model Development, 16, 2737–2752, https://doi.org/10.5194/gmd-16-2737-2023,
825 2023.

Joss, J., Schädler, B., Galli, G., Cavalli, R., Boscacci, M., Held, E., Bruna, G. D., Kappenberger, G., Nespor, V., and Spiess, R.: Operational Use of Radar for Precipitation Measurements in Switzerland, vdf Hochschulverlag AG, ETH Zurich, Switzerland, 1998.

Kong, D., Zhi, X., Ji, Y., Yang, C., Wang, Y., Tian, Y., Li, G., and Zeng, X.: Precipitation Nowcasting Based on Deep Learning over Guizhou, China, Atmosphere, 14, 807, https://doi.org/10.3390/atmos14050807, 2023.

830 Kuhn, H. W.: The Hungarian Method for the Assignment Problem, Naval Research Logistics Quarterly, 2, 83–97, https://doi.org/10.1002/nav.3800020109, 1955.

Leinonen, J., Hamann, U., Nerini, D., Germann, U., and Franch, G.: Latent Diffusion Models for Generative Precipitation Nowcasting with Accurate Uncertainty Quantification, 2023.

Li, L., He, Z., Chen, S., Mai, X., Zhang, A., Hu, B., Li, Z., and Tong, X.: Subpixel-Based Precipitation Nowcasting with the Pyramid
835 Lucas–Kanade Optical Flow Technique, Atmosphere, 9, 260, https://doi.org/10.3390/atmos9070260, 2018.

Li, L., Li, Y., and Li, Z.: Object-Based Tracking of Precipitation Systems in Western Canada: The Importance of Temporal Resolution of Source Data, Clim Dyn, 55, 2421–2437, https://doi.org/10.1007/s00382-020-05388-y, 2020.

Limpert, G., Houston, A., and Lock, N.: The Advanced Algorithm for Tracking Objects (AALTO): Advanced Algorithm for Tracking Objects, Met. Apps, 22, 694–704, https://doi.org/10/f7z6jx, 2015.

840 Lu, M., Li, Y., Yu, M., Zhang, Q., Zhang, Y., Liu, B., and Wang, M.: Spatiotemporal Prediction of Radar Echoes Based on ConvLSTM and Multisource Data, Remote Sensing, 15, 1279, https://doi.org/10.3390/rs15051279, 2023.

Lucas, B. D. and Kanade, T.: An Iterative Image Registration Technique with an Application to Stereo Vision, in: Proceedings of the 1981 DARPA Imaging Understanding Workshop, pp. 121–130, 1981.

Marzban, C., Sandgathe, S., Lyons, H., and Lederer, N.: Three Spatial Verification Techniques: Cluster Analysis, Variogram, and Optical
845 Flow, Wea. Forecasting, 24, 1457–1471, https://doi.org/10/cgxkbc, 2009.

Micheas, A. C., Fox, N. I., Lack, S. A., and Wikle, C. K.: Cell Identification and Verification of QPF Ensembles Using Shape Analysis Techniques, Journal of Hydrology, 343, 105–116, https://doi.org/10/b93xmm, 2007.

Mittermaier, M. P. and Bullock, R.: Using MODE to Explore the Spatial and Temporal Characteristics of Cloud Cover Forecasts from High-Resolution NWP Models, Meteorological Applications, 20, 187–196, https://doi.org/10.1002/met.1393, 2013.

850 Nerini, D., Pulkkinen, S., Hortal, A. P., Velasco, C., Foresti, L., Imhoff, R., Pulkkinen, S., Feldmann, M., Buekenhout, D., Ghaemi, E., Karsisto, P., chiara-arpae, Badger, C., Fangyh09, Ritvanen, J., Joep1999, Cruz, L. D., Rombeek, N., Karsisto, P., aitaten, Carpentieri, A., and mpvginde: pySTEPS/Pysteps: Pysteps v1.8.0, Zenodo, https://doi.org/10.5281/zenodo.10411141, 2023.

Nerini, D., Pulkkinen, S., Hortal, A. P., Velasco, C., Foresti, L., Imhoff, R., Pulkkinen, S., EsmailGhaemi, Feldmann, M., mpvginde, chiara-arpae, Karsisto, P., Buekenhout, D., Badger, C., Fangyh09, Ritvanen, J., Joep1999, Cruz, L. D., NathalieRombeek, Karsisto, P., aitaten,
855 and Carpentieri, A.: ritvje/pysteps: T-DaTing with splits & merges, Zenodo, https://doi.org/10.5281/zenodo.11242613, 2024.

Newman, K. M., Brown, B., Gotway, J. H., Bernardet, L., Biswas, M., Jensen, T., and Nance, L.: Advancing Tropical Cyclone Precipitation Forecast Verification Methods and Tools, Weather and Forecasting, 38, 1589–1603, https://doi.org/10.1175/WAF-D-23-0001.1, 2023.

Pan, X., Lu, Y., Zhao, K., Huang, H., Wang, M., and Chen, H.: Improving Nowcasting of Convective Development by Incorporating Polarimetric Radar Variables Into a Deep-Learning Model, Geophys. Res. Lett., 48, e2021GL095 302, https://doi.org/10/gpbg5d, 2021.

860 Paszke, A., Gross, S., Massa, F., Lerer, A., Bradbury, J., Chanan, G., Killeen, T., Lin, Z., Gimelshein, N., Antiga, L., Desmaison, A., Kopf, A., Yang, E., DeVito, Z., Raison, M., Tejani, A., Chilamkurthy, S., Steiner, B., Fang, L., Bai, J., and Chintala, S.: PyTorch: An Imperative Style, High-Performance Deep Learning Library, in: Advances in Neural Information Processing Systems, vol. 32, Curran Associates, Inc., 2019.

Pulkkinen, S., Chandrasekar, V., and Harri, A.-M.: Nowcasting of Precipitation in the High-Resolution Dallas–Fort Worth (DFW) Urban
865 Radar Remote Sensing Network, IEEE Journal of Selected Topics in Applied Earth Observations and Remote Sensing, 11, 2773–2787, https://doi.org/10.1109/JSTARS.2018.2840491, 2018.

Pulkkinen, S., Chandrasekar, V., and Harri, A.-M.: Fully Spectral Method for Radar-Based Precipitation Nowcasting, IEEE Journal of Selected Topics in Applied Earth Observations and Remote Sensing, 12, 14, 2019a.

Pulkkinen, S., Nerini, D., Pérez Hortal, A. A., Velasco-Forero, C., Seed, A., Germann, U., and Foresti, L.: Pysteps: An Open-Source Python
870 Library for Probabilistic Precipitation Nowcasting (v1.0), Geosci. Model Dev., 2019, 4185–4219, https://doi.org/10/ghmfhd, 2019b.

Pulkkinen, S., Chandrasekar, V., von Lerber, A., and Harri, A.-M.: Nowcasting of Convective Rainfall Using Volumetric Radar Observations, IEEE Trans. Geosci. Remote Sensing, pp. 1–15, https://doi.org/10/ggsw7s, 2020.

Pulkkinen, S., Chandrasekar, V., and Niemi, T.: Lagrangian Integro-Difference Equation Model for Precipitation Nowcasting, Journal of Atmospheric and Oceanic Technology, 38, 2125–2145, https://doi.org/10.1175/JTECH-D-21-0013.1, 2021.

875 pySTEPS developers: pySTEPS/Pysteps: Python Framework for Short-Term Ensemble Prediction Systems [Code], 2023.

Ravuri, S. V., Lenc, K., Willson, M., Kangin, D., Remi Lam, Lam, R., Mirowski, P., Fitzsimons, M., Athanassiadou, M., Kashem, S., Madge, S., Rachel Prudden, Prudden, R., Amol Mandhane, Mandhane, A., Clark, A., Brock, A., Simonyan, K., Hadsell, R., Robinson, N. H., Clancy, E., Alberto Arribas, and Mohamed, S.: Skilful Precipitation Nowcasting Using Deep Generative Models of Radar, Nature, 597, 672–677, https://doi.org/10/gmx6dc, 2021.

880 Raynaud, L., Pechin, I., Arbogast, P., Rottner, L., and Destouches, M.: Object-Based Verification Metrics Applied to the Evaluation and Weighting of Convective-Scale Precipitation Forecasts, Quarterly Journal of the Royal Meteorological Society, 145, 1992–2008, https://doi.org/10.1002/qj.3540, 2019.

Ritvanen, J.: fmidev/lagrangian-convolutional-neural-network: L-CNN model with Swiss data [code], Zenodo, https://doi.org/10.5281/zenodo.11242483, 2024a.

885 Ritvanen, J.: fmidev/nowcast-verification-cell-tracking: Cell tracking -based verification framework for nowcasts [code], Zenodo, https://doi.org/10.5281/zenodo.14227567, 2024b.

Ritvanen, J., Harnist, B., Aldana, M., Mäkinen, T., and Pulkkinen, S.: Advection-Free Convolutional Neural Network for Convective Rainfall Nowcasting, IEEE Journal of Selected Topics in Applied Earth Observations and Remote Sensing, 16, 1654–1667, https://doi.org/10.1109/JSTARS.2023.3238016, 2023.

890 Ritvanen, J., Pulkkinen, S., Moisseev, D., and Nerini, D.: Data for the manuscript the manuscript "Cell tracking -based framework for assessing nowcasting model skill in reproducing growth and decay of convective rainfall" by Ritvanen et al. [data set], https://doi.org/10.57707/fmi-b2share.627e6133c2594dc3945d14fe0ef9c922, 2024a.

Ritvanen, J., Pulkkinen, S., Moisseev, D., and Nerini, D.: Results for the manuscript "Cell tracking -based framework for assessing nowcasting model skill in reproducing growth and decay of convective rainfall" by Ritvanen et al. [data set], https://doi.org/10.57707/fmi-
895 b2share.e1897cfb9a9d4466bb9d7235882bc511, 2024b.

Roberts, N. M. and Lean, H. W.: Scale-Selective Verification of Rainfall Accumulations from High-Resolution Forecasts of Convective Events, Mon. Wea. Rev., 136, 78–97, https://doi.org/10/fn58w4, 2008.

Rosenfeld, D.: Objective Method for Analysis and Tracking of Convective Cells as Seen by Radar, Journal of Atmospheric and Oceanic Technology, 4, 422–434, https://doi.org/10.1175/1520-0426(1987)004<0422:OMFAAT>2.0.CO;2, 1987.

900 Schaefer, J. T.: The Critical Success Index as an Indicator of Warning Skill, Weather and Forecasting, 5, 570–575, https://doi.org/10.1175/1520-0434(1990)005<0570:TCSIAA>2.0.CO;2, 1990.

Seed, A. W.: A Dynamic and Spatial Scaling Approach to Advection Forecasting, Journal of Applied Meteorology and Climatology, 42, 381–388, https://doi.org/10/brsrnc, 2003.

Shi, X., Chen, Z., Wang, H., Yeung, D. Y., Wong, W. K., and Woo, W. C.: Convolutional LSTM network: A machine learning approach
905 for precipitation nowcasting, in: Advances in Neural Information Processing Systems, vol. 2015-January, pp. 802–810, ISSN 1049-5258, 2015.

Shi, X., Gao, Z., Lausen, L., Wang, H., Yeung, D.-Y., Wong, W.-k., and WOO, W.-c.: Deep Learning for Precipitation Nowcasting: A Benchmark and A New Model, in: Advances in Neural Information Processing Systems, vol. 30, Curran Associates, Inc., 2017.

Sønderby, C. K., Espeholt, L., Heek, J., Dehghani, M., Oliver, A., Salimans, T., Agrawal, S., Hickey, J., and Kalchbrenner, N.: MetNet: A
910 Neural Weather Model for Precipitation Forecasting, arXiv:2003.12140 [physics, stat], 2020.

Trebing, K., Stańczyk, T., and Mehrkanoon, S.: SmaAt-UNet: Precipitation Nowcasting Using a Small Attention-UNet Architecture, Pattern Recognition Letters, 145, 178–186, https://doi.org/10.1016/j.patrec.2021.01.036, 2021.

van der Walt, S. J., Schönberger, J. L., Nunez-Iglesias, J., Boulogne, F., Warner, J. D., Yager, N., Gouillart, E., and Yu, T.: Scikit-Image: Image Processing in Python, PeerJ, 2, e453, https://doi.org/10.7717/peerj.453, 2014.

915 Virtanen, P., Gommers, R., Oliphant, T. E., Haberland, M., Reddy, T., Cournapeau, D., Burovski, E., Peterson, P., Weckesser, W., Bright, J., van der Walt, S. J., Brett, M., Wilson, J., Millman, K. J., Mayorov, N., Nelson, A. R. J., Jones, E., Kern, R., Larson, E., Carey, C. J., Polat, İ., Feng, Y., Moore, E. W., VanderPlas, J., Laxalde, D., Perktold, J., Cimrman, R., Henriksen, I., Quintero, E. A., Harris, C. R., Archibald, A. M., Ribeiro, A. H., Pedregosa, F., and van Mulbregt, P.: SciPy 1.0: Fundamental Algorithms for Scientific Computing in Python, Nature Methods, 17, 261–272, https://doi.org/10.1038/s41592-019-0686-2, 2020.

920 Wen, Y., Zhang, J., Wang, D., Wang, C., and Wang, P.: Research on Radar Echo Extrapolation Method by Fusing Environment Grid Point Field Information, Atmosphere, 14, 980, https://doi.org/10.3390/atmos14060980, 2023.

Wernli, H., Paulat, M., Hagen, M., and Frei, C.: SAL—A Novel Quality Measure for the Verification of Quantitative Precipitation Forecasts, Mon. Wea. Rev., 136, 4470–4487, https://doi.org/10/fprx82, 2008.

World Meteorological Organization: Guidelines for Nowcasting Techniques, Tech. Rep. WMO-No.1198, World Meteorological Organiza-
925 tion, Geneva, Switzerland, ISBN 978-92-63-11198-2, 2017.

Zahraei, A., Hsu, K.-l., Sorooshian, S., Gourley, J. J., Lakshmanan, V., Hong, Y., and Bellerby, T.: Quantitative Precipitation Nowcasting: A Lagrangian Pixel-Based Approach, Atmospheric Research, 118, 418–434, https://doi.org/10.1016/j.atmosres.2012.07.001, 2012.

Zan, B., Yu, Y., Li, J., Zhao, G., Zhang, T., and Ge, J.: Solving the Storm Split-Merge Problem—A Combined Storm Identification, Tracking Algorithm, Atmospheric Research, 218, 335–346, https://doi.org/10/gf52zh, 2019.

930 Zhang, F., Wang, X., and Guan, J.: A Novel Multi-Input Multi-Output Recurrent Neural Network Based on Multimodal Fusion and Spatiotemporal Prediction for 0–4 Hour Precipitation Nowcasting, Atmos., 12, 1596, https://doi.org/10/gpbppc, 2021.

Zhang, Y., Long, M., Chen, K., Xing, L., Jin, R., Jordan, M. I., and Wang, J.: Skilful Nowcasting of Extreme Precipitation with NowcastNet, Nature, 619, 526–532, https://doi.org/10.1038/s41586-023-06184-4, 2023.

Zheng, K., Liu, Y., Zhang, J., Luo, C., Tang, S., Ruan, H., Tan, Q., Yi, Y., and Ran, X.: GAN–argcPredNet v1.0: A Generative Adversar-
935 ial Model for Radar Echo Extrapolation Based on Convolutional Recurrent Units, Geoscientific Model Development, 15, 1467–1475, https://doi.org/10.5194/gmd-15-1467-2022, 2022.

Zhu, K., Chen, H., and Han, L.: MCT U-net: A Deep Learning Nowcasting Method Using Dual-polarization Radar Observations, in: IGARSS 2022 - 2022 IEEE International Geoscience and Remote Sensing Symposium, pp. 4665–4668, ISSN 2153-7003, https://doi.org/10.1109/IGARSS46834.2022.9884871, 2022.